

## A Spectroscopic Search for Dormant Black Holes in Low-Metallicity Binaries

PRANAV NAGARAJAN ,<sup>1</sup> KAREEM EL-BADRY ,<sup>1</sup> HENRIQUE REGGIANI ,<sup>2</sup> CASEY Y. LAM ,<sup>3</sup> JOSHUA D. SIMON ,<sup>3</sup>  
 JOHANNA MÜLLER-HORN ,<sup>4</sup> RHYS SEEBURGER ,<sup>4</sup> HANS-WALTER RIX ,<sup>4</sup> HOWARD ISAACSON ,<sup>5</sup> JESSICA LU ,<sup>5</sup>  
 VEDANT CHANDRA ,<sup>6</sup> AND RENE ANDRAE <sup>4</sup>

<sup>1</sup>Department of Astronomy, California Institute of Technology, 1200 E. California Blvd., Pasadena, CA 91125, USA

<sup>2</sup>Gemini Observatory/NSF's NOIRLab, Casilla 603, La Serena, Chile

<sup>3</sup>Observatories of the Carnegie Institution for Science, 813 Santa Barbara St., Pasadena, CA 91101, USA

<sup>4</sup>Max Planck Institute for Astronomy, Königstuhl 17, D-69117, Heidelberg, Germany

<sup>5</sup>Department of Astronomy, University of California, Berkeley, Berkeley, CA, 94720, USA

<sup>6</sup>Center for Astrophysics | Harvard & Smithsonian, 60 Garden Street, Cambridge, MA 02138, USA

### ABSTRACT

The discovery of the massive black hole (BH) system Gaia BH3 in pre-release *Gaia* DR4 data suggests that wide BH binaries with luminous companions may be significantly overrepresented at low metallicities. Motivated by this finding, we have initiated a spectroscopic survey of low-metallicity stars exhibiting elevated RUWE values in *Gaia* DR3, using the FEROS and APF spectrographs. We identify promising BH binary candidates as objects with instantaneously measured radial velocities (RVs) that are very different from their mean RVs reported in *Gaia* DR3. Thus far, we have observed over 500 targets, including a nearly complete sample of stars with  $[\text{Fe}/\text{H}] < -1.5$ ,  $\text{RUWE} > 2$ , and  $G < 15$ . Our search has yielded one promising target exhibiting slow acceleration and an RV more than  $98 \text{ km s}^{-1}$  different from its DR3 mean RV, as well as dozens of other candidates with smaller RV discrepancies. We quantify the sensitivity of our search using simulations, demonstrating that it recovers at least half of the BH companions within our selection criteria. We make all the spectra and RVs from our survey publicly available and encourage further follow-up.

*Keywords:* Stellar astronomy (1583), Black holes (162)

### 1. INTRODUCTION

The Milky Way (MW) is thought to contain  $\sim 10^8$  stellar-mass black holes (BHs; e.g., A. Olejak et al. 2020). Only a tiny fraction of this population has been discovered, as BH searches are severely affected by observational incompleteness. For five decades, the only known Galactic BHs were in close binaries that shine brightly in X-rays due to accretion (e.g., J. M. Corral-Santana et al. 2016). However, these X-ray binaries are a rare outcome of binary evolution, and are expected to be vastly outnumbered by both wider binaries hosting non-accreting (“dormant”) BHs (e.g., S. F. Portegies Zwart et al. 1997; C. Chawla et al. 2022) and isolated BHs (e.g., C. Y. Lam et al. 2022; K. C. Sahu et al. 2022).

The *Gaia* mission (Gaia Collaboration et al. 2016) has opened a new window on the population of rare binaries in the Milky Way, with the mission’s 3rd data release (“DR3”, Gaia Collaboration et al. 2023a) increasing the number of well-characterized binary orbits by more than an order of magnitude (Gaia Collaboration et al. 2023b).

Email: pnagaraj@caltech.edu

*Gaia* produces catalogs of photometrically, spectroscopically, and astrometrically variable binaries (Gaia Collaboration et al. 2023b; N. Mowlavi et al. 2023; R. Gomel et al. 2023; L. Eyer et al. 2023; J.-L. Halbwachs et al. 2023), and several recent studies have searched for dormant BHs in these catalogs (e.g., K. El-Badry & H.-W. Rix 2022; S. Shahaf et al. 2023; P. Nagarajan et al. 2023). In contrast to most other methods, *Gaia* astrometry is most sensitive to binaries with relatively wide orbits (e.g., J.-L. Halbwachs et al. 2023; K. El-Badry 2024). Notably, DR3 astrometry has led to the discovery and characterization of two nearby dormant BHs (“Gaia BHs”, K. El-Badry et al. 2023a; S. Chakrabarti et al. 2023; P. Nagarajan et al. 2024b; A. Tanikawa et al. 2023; K. El-Badry et al. 2023b) and a population of dormant neutron stars (NSs) (“Gaia NSs”, K. El-Badry et al. 2024a,b) in au-scale orbits. Population synthesis studies calibrated to the DR3 detections predict discovery of dozens more Gaia BHs in future data releases (e.g., P. Nagarajan et al. 2025).

Recently, Gaia Collaboration et al. (2024) announced the discovery of Gaia BH3, a  $33 M_{\odot}$  BH orbited by a  $0.8 M_{\odot}$  red giant in an 11.6 yr orbit, in pre-

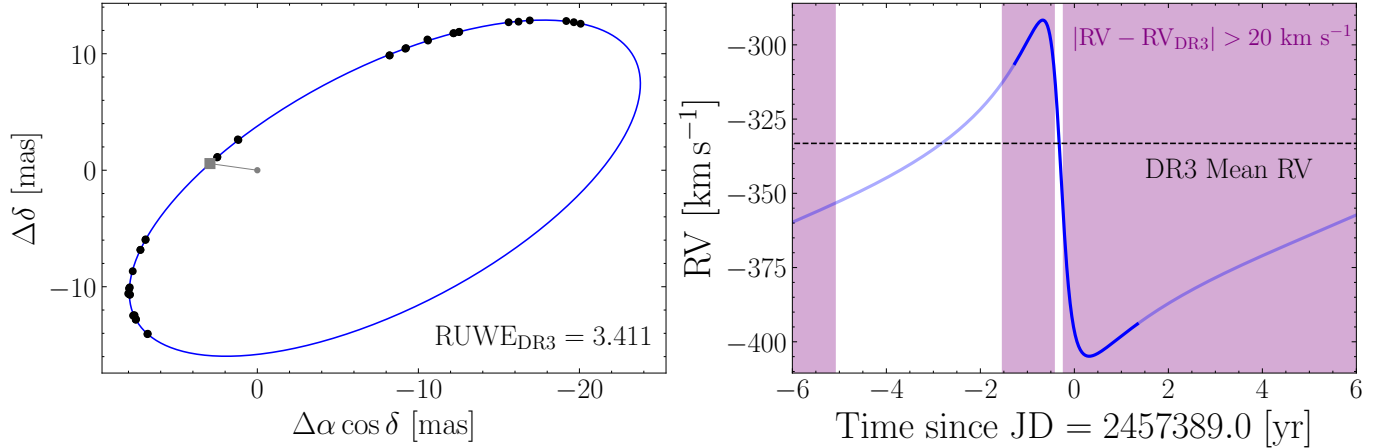


**Figure 1.** Simulated *Gaia* DR3 epoch astrometry and radial velocity curve for Gaia BH3 based on best-fit combined parameters from [Gaia Collaboration et al. \(2024\)](#). In the left panel, the gray line connects the barycenter to periastron. In the right panel, the temporal range of the simulated DR3 epoch astrometry is plotted with higher opacity. The epoch RVs of Gaia BH3 are different from its reported mean RV by at least  $20 \text{ km s}^{-1}$  over  $\sim 70\%$  of its orbit (shaded purple region), suggesting that a search strategy based on this comparison may be useful in finding similar targets.

release astrometry from the mission’s 4th data release (“DR4”). Gaia BH3 hosts the most massive known stellar-mass BH in the Milky Way, and the lowest-metallicity ( $[\text{Fe}/\text{H}] = -2.56$ , see also [E. Balbinot et al. 2024](#)) luminous companion to a BH, providing empirical evidence that low-metallicity massive stars leave behind massive BHs. Because Gaia BH3 is in the typical mass range of the merging BHs detected via gravitational waves (GWs) at extragalactic distances (e.g., [R. Abbott et al. 2023](#)), the system also provides tantalizing evidence that low-metallicity massive stars are the progenitors of GW events.

Since Gaia BH3 is relatively bright ( $G = 11.2$ ), there may be many similar, but fainter, systems waiting to be discovered. Indeed, for a Kroupa initial mass function (IMF) ([P. Kroupa 2001](#)), there are  $\sim 10^2$  times more low-mass metal-poor main sequence stars in our solar neighborhood than there are red giants similar to the companion star in Gaia BH3. Hence, even within 590 pc (the distance to Gaia BH3), there likely exist other massive BHs that are orbited by metal-poor stars still on the main sequence. At the distance and extinction of Gaia BH3, such companions would have  $G < 15$  for  $M \gtrsim 0.67 M_\odot$ , readily accessible to *Gaia* astrometry and spectroscopic follow-up.

Even though we do not know the exact selection function that yielded the three known Gaia BHs, luminous companions to Gaia BHs (and Gaia NSs, see [K. El-Badry et al. 2024b](#)) appear to be significantly overrepresented at low metallicity ([K. El-Badry 2024](#)). Indeed, based on the Gaia XP metallicity catalog of [R. Andrae et al. \(2023\)](#), only 1 in  $10^4$  giants in the solar neighborhood is as metal-poor as Gaia BH3, and Gaia BH3 is among the  $\approx 25$  nearest giants of such low metallicity. Why wide BH and NS companions might be overrepresented at low metallicity is an open question.

One possibility is that low-metallicity massive stars remain more compact in their post-main-sequence evolution than solar-metallicity stars of the same initial mass (e.g., [A. Maeder 1987](#); [P. Marchant et al. 2016](#); [J. Klencki et al. 2020](#)). While solar-metallicity BH progenitors expand to become red supergiants and engulf their stellar companions, very low-metallicity massive stars may not expand as much, allowing a larger fraction of binaries to survive and producing more BH + low-mass star binaries (e.g., [G. Iorio et al. 2024](#)).

Previous studies have exhaustively searched the catalog of DR3 orbital solutions for dormant BHs and NSs in wide orbits ([J. J. Andrews et al. 2022](#); [S. Shahaf et al. 2023](#); [K. El-Badry et al. 2023a,b, 2024a,b](#)). In this work, we perform spectroscopic follow-up on a sample of low-metallicity stars with acceleration solutions or high astrometric excess noise (Renormalized Unit Weight Error, or “RUWE”) values in *Gaia* DR3, indicating binarity. This investigation cannot be carried out with *Gaia* data alone. *Gaia* DR3 includes mean radial velocities (RVs) for stars with  $G_{\text{RVS}} \lesssim 14$ , but these represent an average RV measured from spectra coadded over several years ([D. Katz et al. 2023](#)). Epoch-level RVs are only measured for stars with  $G_{\text{RVS}} \lesssim 12$ , and are not included in the DR3 catalog ([D. Katz et al. 2023](#)). External, time-resolved RVs are thus crucial for constraining the possible nature of the companions.

In Section 2, we describe and motivate our search method. In Section 3, we detail our sample selection process. In Section 4, we describe the spectra obtained from our follow-up campaign. In Section 5, we analyze the collected RVs and identify promising compact object candidates for further follow-up. We discuss the completeness and expected yields of our search in Section 6. Finally, we summarize our results in Section 7.

## 2. MOTIVATION

We design our search to be sensitive to Gaia BH3-like binaries. We use the `gaiamock` code (K. El-Badry et al. 2024), which forward-models *Gaia* epoch astrometry and model fitting, to simulate epoch astrometry and a radial velocity (RV) curve for Gaia BH3 as it would have been observed in *Gaia* DR3. We show the epoch astrometry and RV curve in Figure 1, with times provided relative to the DR3 reference epoch of Julian Date (JD) = 2457389.0. The epoch astrometry was insufficiently constraining for Gaia BH3 to receive an orbital solution in DR3. However, the source had RUWE = 3.4, indicative of a poor single-star astrometric fit (L. Lindegren 2018). In addition, the star’s RV is predicted to be different from the reported mean RV in DR3 by  $\geq 20 \text{ km s}^{-1}$  over  $\sim 70\%$  of its orbit. This suggests that a search strategy based on measuring epoch RVs for low-metallicity stars with high RUWE values in DR3, and comparing those RVs to the corresponding mean RVs reported in DR3, could lead to the discovery of BH or NS binaries that did not receive orbital solutions in DR3.

To explore what types of BH binaries can be detected via elevated RUWE, we investigate the variation of RUWE with orbital period, distance, and BH mass. We randomly sample sky positions from our catalog of candidate low-metallicity binaries (see Section 3), orbital eccentricities from a thermal distribution, and isotropic binary orientations. We adopt default values of  $P_{\text{orb}} = 10^3 \text{ d}$ ,  $d = 1 \text{ kpc}$ , and  $M_{\text{BH}} = 10 M_{\odot}$ , typical of binaries that our search strategy is sensitive to, and predict the RUWE in DR3 using `gaiamock`. We vary one quantity at a time in each panel in Figure 2. We plot curves separately for dwarfs and giants, assuming absolute magnitudes of  $M_G = 4$  for dwarfs and  $M_G = 0$  for giants. Initially, RUWE increases as the orbital period and projected semi-major axis of the photocenter increase, peaking at  $\sim 10^3$  days. At  $> 10^3 \text{ d}$ , however, DR3’s limited observing baseline causes RUWE to decrease with orbital period instead. RUWE also decreases as the distance to a binary increases, since this causes the projected semi-major axis of the photocenter to decrease. RUWE is only weakly sensitive to BH mass.

In general, giants lead to slightly larger RUWE values than dwarfs. However, the behavior of the curves in Figure 2 is determined by how the epoch astrometry uncertainties vary with apparent  $G$ -band magnitude. The uncertainties are smallest at  $G = 8\text{--}14$ , and rise at brighter or fainter magnitudes outside this range (B. Holl et al. 2023). This leads to a somewhat non-intuitive dependence of RUWE on distance in Figure 2. As sources become too bright, uncertainties rise and RUWE falls, causing giants to have smaller RUWE values than dwarfs at close distances. Companions to giants are more detectable than companions to dwarfs only at large distances ( $d \gtrsim 1.5 \text{ kpc}$ ), because the uncertainties for dwarfs increase rapidly at those distances.

Our main sample includes a selection cut of  $\text{RUWE} > 2.0$  (see Section 3 for details). This implies that we are sensitive to orbital periods of 100–5000 d and distances out to  $\sim 2 \text{ kpc}$ .

## 3. SAMPLE SELECTION

We select candidate metal-poor binaries using two sets of simple cuts on RUWE and the metallicity. We adopt the data-driven metallicities derived by R. Andrae et al. (2023), who use the XGBoost algorithm (T. Chen & C. Guestrin 2016) to infer stellar parameters from low-resolution *Gaia* XP spectra. These metallicities are reliable because R. Andrae et al. (2023) train their model on externally derived, high-fidelity stellar parameters from APOGEE (Abdurro’uf et al. 2022) and augment their training data with a set of very-metal-poor stars that have [M/H] values similar to those in our sample. R. Andrae et al. (2023) also use cross-validation to demonstrate the reliability of their model predictions.

### 3.1. $[\text{M}/\text{H}] < -1.5$ sample

We selected all sources from the R. Andrae et al. (2023) catalog with  $[\text{M}/\text{H}] < -1.5$ ,  $\text{RUWE} > 2.0$ , and the following quality cuts:

- Apparent magnitude  $G < 15$ , to allow for RV measurement with small telescopes.
- parallax  $\varpi > 0.5 \text{ mas}$ , corresponding to a distance limit of  $\lesssim 2 \text{ kpc}$ .
- `ipd_frac_multi_peak`  $< 3$ , to exclude marginally resolved wide binaries with elevated RUWE due to blending rather than orbital motion (L. Lindegren 2022).
- Color  $0.3 < G_{\text{BP}} - G_{\text{RP}} < 2.5$ , to exclude hot and cool stars for which the metallicities from R. Andrae et al. (2023) are unlikely to be reliable.
- $v_{\perp} > 70 \text{ km s}^{-1}$ , where  $v_{\perp} = 4.74 \text{ km s}^{-1} \times (\mu/\text{mas yr}^{-1})/(\varpi/\text{mas})$  is the source’s tangential velocity, and  $\mu$  is the source’s total proper motion. This excludes sources with disk-like kinematics, which are more likely to be metal-rich contaminants.
- A measured radial velocity in *Gaia* DR3, so that an RV change can be measured.
- `rv_amplitude_robust`  $> 15 \text{ km s}^{-1}$ , excluding sources with small RV shifts measured during the DR3 observing baseline. This cut applies only to the minority of sources with  $G_{\text{RVS}} < 12$ , for which epoch RVs were measured in DR3.

These cuts yielded a total of 595 sources. Of these, 139 already have an orbital solution reported in the `gaiadr3.nss_two_body_orbit` catalog. Most of these

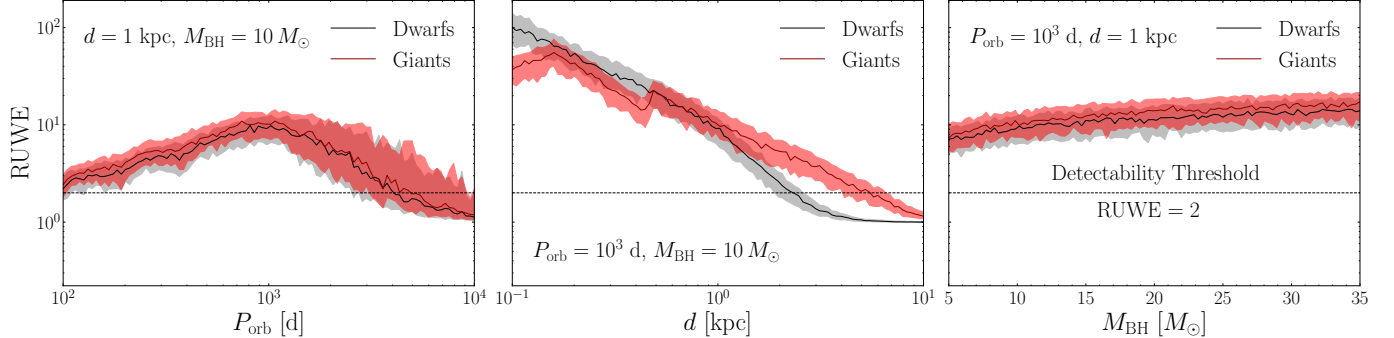


**Figure 2.** Dependence of predicted RUWE in DR3 on orbital period, distance, and BH mass for low-metallicity dwarf or giant companions to BHs, with the shaded regions representing a 68% confidence interval. We randomly sample sky positions from our catalog of candidates, orbital eccentricities from a thermal distribution, and isotropic binary orientations. At orbital periods of  $10^2$ – $10^3$  d, RUWE increases as the projected semi-major axis of the photocenter increases, peaking at  $\sim 10^3$  days. At orbital periods  $> 10^3$  d, the limited orbital coverage during *Gaia* DR3’s  $\sim 1000$  d observing baseline causes RUWE to decrease. RUWE also decreases as the binary gets farther away, since the projected semi-major axis of the photocenter decreases. RUWE is only weakly sensitive to BH mass. Due to their brighter absolute magnitudes, giants tend to have slightly larger RUWE values than dwarfs, and are detectable out to farther distances. With a selection cut of  $\text{RUWE} > 2.0$ , we are sensitive to orbital periods of 100–5000 d and distances out to  $\sim 2$  kpc.

are astrometric Orbital solutions and have been investigated elsewhere (e.g., A. Tanikawa et al. 2023; K. El-Badry et al. 2023b). None imply massive dark companions.

We measured at least one RV for 423 of the remaining 456 candidates. We have thus observed  $\approx 93\%$  of the remaining 456 objects in the  $[\text{M}/\text{H}] < -1.5$  sample, or  $\approx 94\%$  of 595 when we include the objects with orbital solutions. Of the 456 candidates lacking orbital solutions, 108 have acceleration or variable acceleration solutions reported in the `gaiadr3.nss_acceleration_astro` catalog. 102 of these sources are in our observed sample. The acceleration solutions suggest that these are long-period ( $\gtrsim 500$  d; K. El-Badry et al. 2024) binaries, but are insufficient to constrain the companion masses on their own.

### 3.2. $[\text{M}/\text{H}] < -1$ , large $a_0$ sample

Once most of the  $[\text{M}/\text{H}] < -1.5$  sample had been observed, we selected additional metal-poor candidates with a selection designed to prioritize large photocenter orbits. We began by selecting sources with  $[\text{M}/\text{H}] < -1.0$  according to R. Andrae et al. (2023) and  $\text{RUWE} > 1.4$ , and applied the same cuts on  $G$ ,  $\varpi$ ,  $v_\perp$ , `ipd_frac_multi_peak`, DR3 RV, color, and `rv_amplitude_robust` that are used in the  $[\text{M}/\text{H}] < -1.5$  sample. We removed any overlapping sources that were already present in the  $[\text{M}/\text{H}] < -1.5$  sample.

Motivated by K. El-Badry et al. (2024) (their Figure 8), we predict the approximate photocenter orbit semi-major axis of each binary from RUWE as

$$\hat{a}_0 = 2.4\sigma_\eta(G)\sqrt{\text{RUWE}^2 - 1}, \quad (1)$$

where  $\sigma_\eta(G)$  is the along-scan measurement uncertainty per CCD (e.g. Figure 1 of K. El-Badry et al. 2024)

and  $\hat{a}_0$  is a RUWE-informed estimate of the photocenter semi-major axis. We then selected targets satisfying

$$\frac{\hat{a}_0}{\varpi} > 1 \text{ au}. \quad (2)$$

These cuts yielded a total of 292 sources, of which 31 already had an orbital solution reported in the `gaiadr3.nss_two_body_orbit` catalog. As before, these sources have already been investigated elsewhere; none harbor massive dark companions.

Luminous companions yield smaller photocenter orbits at fixed mass than dark companions, and so this selection is designed to target binaries with large photocenter orbits corresponding to dark and massive companions. Equation 1 will underestimate  $a_0$  in cases where the period significantly exceeds the 1000-d DR3 observing baseline, so we expect most binaries selected in this way to have periods of order 1000 d. Given that the binaries’ periods are not known a priori and there is significant scatter in the relation between RUWE and  $a_0$  (C. Y. Lam et al. 2025; K. El-Badry 2025), it is inevitable that some luminous binaries with smaller orbits will enter the sample as well.

We measured at least one RV for 103 of the remaining 261 candidates. We have thus observed  $\approx 39\%$  of the remaining 261 objects in the  $[\text{M}/\text{H}] < -1.0$ , large  $a_0$  sample, or  $\approx 46\%$  of 292 when we include the objects with orbital solutions. Of the 261 candidates lacking orbital solutions, 4 have acceleration or variable acceleration solutions reported in the `gaiadr3.nss_acceleration_astro` catalog. 2 of these sources are in our observed sample.

### 3.3. Summary of the sample

Basic properties of our sample of low-metallicity stars with elevated RUWE are summarized in Figure 3. We

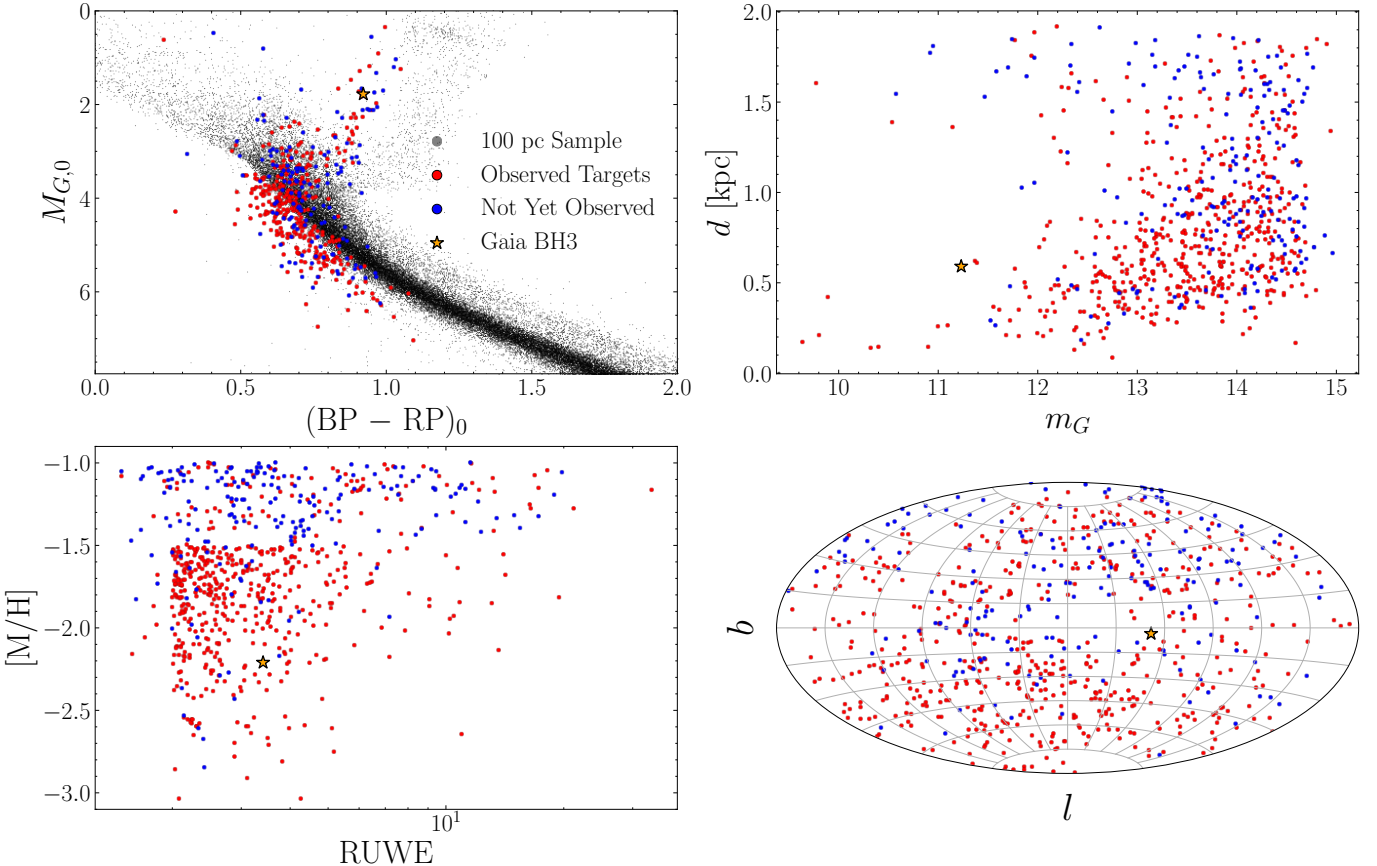


**Figure 3.** Properties of our sample of low-metallicity stars with elevated RUWE, with Gaia BH3 shown for comparison. Upper left: Color-magnitude diagram. As expected, the low-metallicity stars are bluer than their counterparts in the 100 pc random comparison sample. Upper right: Distance versus apparent magnitude for all targets. They are bright and have mean RVs in DR3. Lower left: Metallicity versus RUWE for all targets. They have  $[M/H] < -1$  and high RUWE values indicating binarity. Lower right: Sky distribution of all targets. They are distributed approximately randomly across the sky.

exclude candidates with orbital solutions. In the upper left panel, we show an extinction-corrected color-magnitude diagram, with a random comparison sample of stars within 100 pc for reference. The extinctions are calculated based on reddenings retrieved from the 3D dust map of G. M. Green et al. (2019). As expected, the low-metallicity stars are bluer than the comparison sample. In the upper right panel, we plot distance versus apparent magnitude for all targets. Our targets tend to lie between  $G = 12\text{--}15$  and have typical distances of 0.5–2 kpc. In the lower left panel, we plot metallicity versus RUWE. All observed targets have both  $[M/H] < -1$  and high RUWE values  $> 1.4$  indicating binarity. The structure in this panel arises because we use different sample selection criteria for binaries with  $[M/H] < -1.5$  and  $-1.5 < [M/H] < -1.0$ . Finally, in the lower right, we show the sky distribution of all targets. The targets are distributed approximately randomly, as expected for halo stars. Some structure is evident, perhaps due in part to our cut of  $v_{\perp} > 70 \text{ km s}^{-1}$ , which excludes stars on disk-like orbits.

DR3 parallax uncertainties for sources with elevated RUWE are underestimated by a factor of 1–4 (K. El-Badry 2025). After inflating the parallax uncertainties of our targets based on the prescription of K. El-Badry (2025), we find that  $\approx 68\%$  still have parallax to parallax uncertainty ratios  $> 5$ , implying that this effect does not significantly affect our sample selection or our subset of BH binary candidates displaying large RV variability.

In summary, we obtain at least one epoch RV for a majority of low-metallicity stars with  $[M/H] < -1.5$  and  $\text{RUWE} > 2.0$ . We also obtain epoch RVs for an additional subset of sources with  $[M/H] < -1.0$ ,  $\text{RUWE} > 1.4$ , and large photocenter orbits. Most of the 500+ binaries in our observed sample are expected to have orbital periods  $\gtrsim 10^3$  days, though some are likely shorter-period binaries or higher-order multiples that failed one or more of the quality cuts imposed on DR3 astrometric solutions. DR3 reports mean RVs for stars with  $G_{\text{RVS}} \lesssim 14$  and RV variability information for stars with  $G_{\text{RVS}} \lesssim 12$ . For the typical colors of targets in our sample, these correspond roughly to  $G < 15$  and  $G < 13$ , respectively. A complimentary sample of low-metallicity stars with

potential BH companions will be investigated in Lam et al. (forthcoming).

## 4. DATA

### 4.1. Spectroscopic Follow-up

We obtain 648 spectra for 526 targets,  $\sim 7$  years after the median epoch of the time series data in *Gaia* DR3. We use a typical exposure time of 1800s for targets with  $G = 14$ , and shorter and longer exposure times for brighter and fainter objects.

#### 4.1.1. FEROS

We use the Fiberfed Extended Range Optical Spectrograph (FEROS; A. Kaufer et al. 1999) on the 2.2m ESO/MPG telescope at La Silla Observatory for targets at  $\delta < 20^\circ$  (programs 113.26XB.001, 114.27SS.001, and 115.28KE.001). The resulting spectra have resolution  $R \approx 50,000$  over a spectral range of 350–920 nm, and a typical SNR of 4 at 5178 Å. We reduced the data using the CERES pipeline (R. Brahm et al. 2017). The pipeline performs bias subtraction, flat fielding, wavelength calibration, and optimal extraction, and measures and corrects for small shifts in the wavelength solution over the course of a night using simultaneous observations of a ThAr lamp with a second fiber. For each spectrum, we estimate the continuum using a median filter, and then perform continuum normalization.

#### 4.1.2. APF

We use the Levy spectrometer on the 2.4m Automated Planet Finder (APF; M. V. Radovan et al. 2010; S. S. Vogt et al. 2014) telescope at Lick Observatory for targets at  $\delta \geq 20^\circ$ . We used a 2" slit, yielding spectra with resolution  $R \approx 80,000$  over a wavelength range of 373–1020 nm and a typical SNR of 8 at 5178 Å. We reduced the data using the California Planet Search pipeline (A. W. Howard et al. 2010; B. J. Fulton et al. 2015). As with the FEROS spectra, we estimate the continuum of each spectrum using a median filter, and then perform continuum normalization.

### 4.2. Radial Velocities

We measure RVs via cross-correlating with a synthetic template spectrum. Specifically, we measure RVs based on two consecutive orders that display prominent absorption features. We use orders 9 and 10 for FEROS and orders 34 and 35 for APF, corresponding to wavelength regions of 5048–5362 Å and 5137–5279 Å, respectively. These wavelength regions include the Mg I b triplet, which in most of our targets is among the strongest features in the optical. We experimented with a variety of spectral regions and found these to be the most robust; the Balmer lines are too broad, and the Mg I lines are among the strongest lines in metal-poor stars. Many other orders do not contain detectable lines in most of our targets.

We calculate the chi-squared statistic as a function of RV shift, defined as:

$$\chi^2 = \sum_{\lambda} \left( \frac{F_{\lambda,\text{obs}} - F_{\lambda,\text{template}}}{\sigma_{F_{\lambda,\text{obs}}}} \right)^2, \quad (3)$$

where  $F_{\lambda,\text{obs}}$  is the observed flux,  $F_{\lambda,\text{template}}$  is the template flux, shifted to the appropriate RV, and  $\sigma_{F_{\lambda,\text{obs}}}$  is the uncertainty in the observed flux at wavelength  $\lambda$ .

For each target, we choose the template spectrum as the BOSZ Kurucz (R. L. Kurucz 1979, 1993; S. Mészáros et al. 2024) spectrum with stellar parameters closest to those derived by R. Andrae et al. (2023). The template spectra cover a grid of metallicity  $[\text{M}/\text{H}] \in (-2.5, -1.0)$  spaced by  $-0.25$ , effective temperature  $T_{\text{eff}} \in (4000 \text{ K}, 6500 \text{ K})$  spaced by 250 K, and surface gravity  $\log(g/\text{cm s}^{-2}) \in (2.5, 4.5)$  spaced by 0.5. The template spectra are at a resolution of  $R = 50,000$  and assume no rotational broadening.

The best-fit RV is the shift for which the  $\chi^2$  statistic is minimized. Uncertainties on RVs are derived based on the width of the minimum, i.e., the difference at which the  $\chi^2$  statistic changes by one. All of our RVs are reported in Table 3 in Appendix A.

We manually inspected the template fit in all cases where the epoch RV differed from the mean DR3 RV by more than 10 km s $^{-1}$  (see Table 1). During this vetting process, we visually identified a few objects where a joint fit to both orders produced a less accurate RV than a fit to only one of the orders. In these cases, we adopt the more accurate RV derived from the best fit to one of the orders alone.

We show the observed FEROS spectrum for a typical target, along with the template spectrum used to derive the corresponding best-fit RV, in Figure 4. We plot a spectral region centered on the Mg I b triplet, from which most of the signal used to derive the RV arises. We also show the  $\chi^2$  statistic as a function of RV shift. The location of the minimum in this curve corresponds to the best-fit RV.

### 4.3. Flagged Spectra

We show the observed FEROS spectrum and  $\chi^2$  statistic as a function of RV shift for a target for which the derived RV is unreliable in Figure 5. The  $\chi^2$  statistic curve clearly has two local minima, suggesting that the system is a double-lined spectroscopic binary (i.e., SB2). Visually, the single-star template shifted into the lab frame does not seem to be a good fit to the observed spectrum for either plausible RV.

Some spectra have low signal-to-noise values (i.e.,  $\text{SNR} < 2$  at 5200 Å) or are likely contaminated with moonlight (i.e. have barycenter correction within 10 km s $^{-1}$  of the derived RV). Other spectra do not have prominent absorption lines due to high effective temperatures (i.e., the source is a hot star) or rapid rotation (i.e., the source has a high  $v \sin i$ ). In all these cases, we flag the

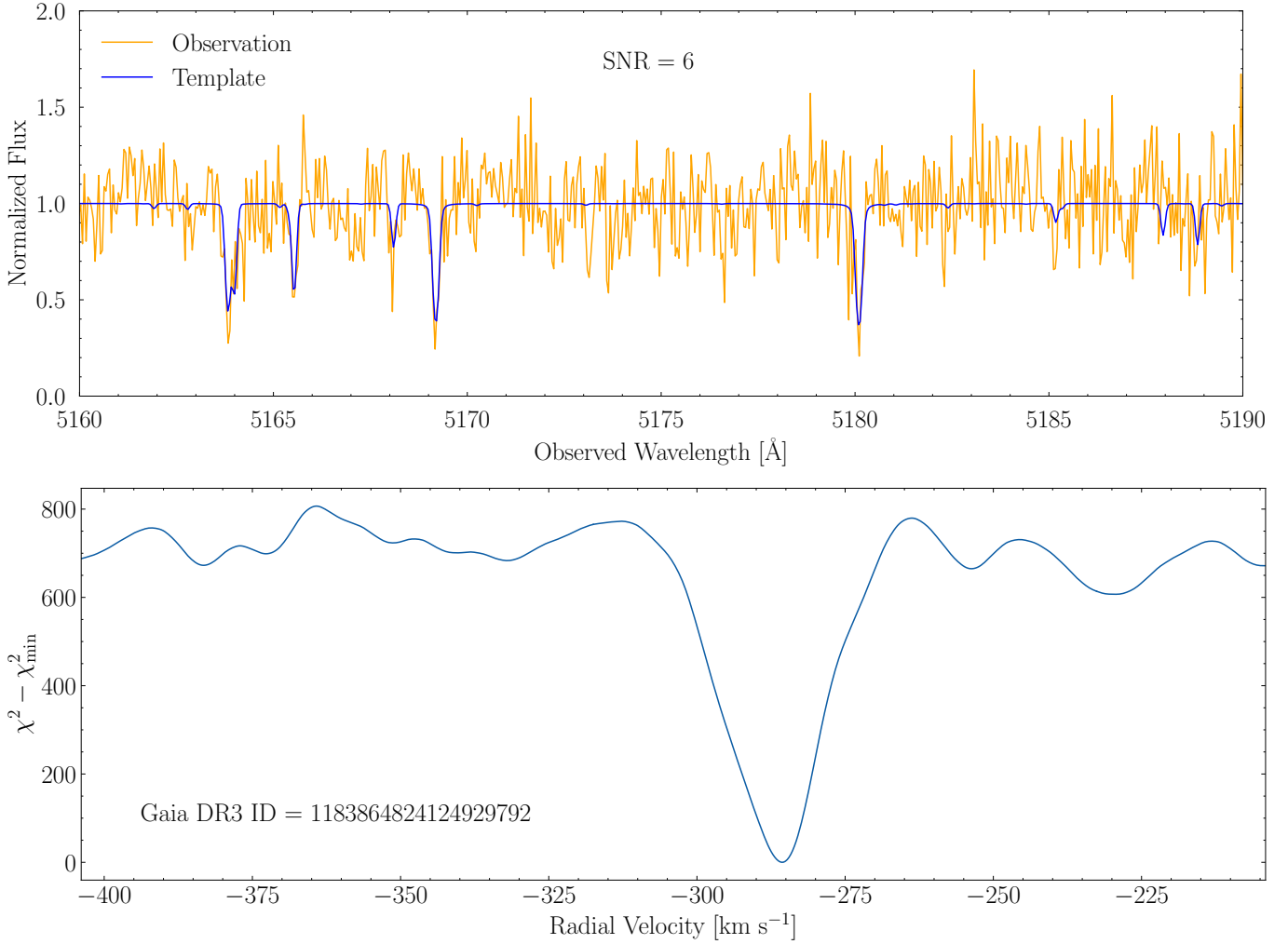


**Figure 4.** Top: Comparison of a template to a FEROS spectrum of a typical target in our sample. The three strongest lines are due to the Mg I b triplet. Bottom: Chi-squared statistic as a function of RV shift for the same target. The minimum corresponds to the derived RV. We measure a robust RV of  $-286.16 \pm 0.45 \text{ km s}^{-1}$  despite the relatively low SNR of 6.

derived RV as unreliable, remove the target from our sample of promising candidates, and report the flag in Table 3.

## 5. RESULTS

We compare our derived RVs to the mean RVs reported in DR3 in the top panel of Figure 6. We plot good RVs in blue, and RVs for spectra that were flagged in orange. We show a residual plot in the bottom panel. In most cases, the epoch RVs are in good agreement with the mean RVs. In several cases, the two RVs are discrepant beyond the statistical uncertainties, suggesting the possibility of a hidden compact object companion.

In Gaia BH3, the star's RV is at least  $20 \text{ km s}^{-1}$  and  $10 \text{ km s}^{-1}$  different from the mean RV published in Gaia DR3 over  $\approx 70\%$  and  $\approx 85\%$  of the orbit, respectively. Since the instantaneously measured RV of a given target is expected to be significantly different from its mean RV over a large portion of its orbit (Figure 1), a large RV shift is potentially indicative of a massive companion.

Conversely, a small RV shift relative to the DR3 mean disfavors a massive companion, though it does not rule one out. We explore this quantitatively in Section 6.

We list all promising (i.e., non-flagged) targets with RV discrepancy  $> 10 \text{ km s}^{-1}$  in Table 1. We have manually vetted each candidate in this table, removing targets that are luminous binaries, hot stars, or fast rotators. Of the 66 interesting candidates that remain, 57 are from the  $[\text{M}/\text{H}] < -1.5$ ,  $\text{RUWE} > 2.0$  sample, while 9 are from the  $[\text{M}/\text{H}] < -1.0$ ,  $\text{RUWE} > 1.4$ , large  $a_0$  sample. We verify that our search method successfully recovers Gaia BH3, which has Gaia DR3 source ID 4318465066420528000. Our search returns 6 non-flagged candidates with maximum RV discrepancies larger than Gaia BH3.

If we account for the uncertainties on our RV measurements and the reported *Gaia* DR3 RVs, only 48 of the 66 interesting candidates listed in Table 1 have RV discrepancies  $> 0$  at the  $2\sigma$  level. However, these uncer-

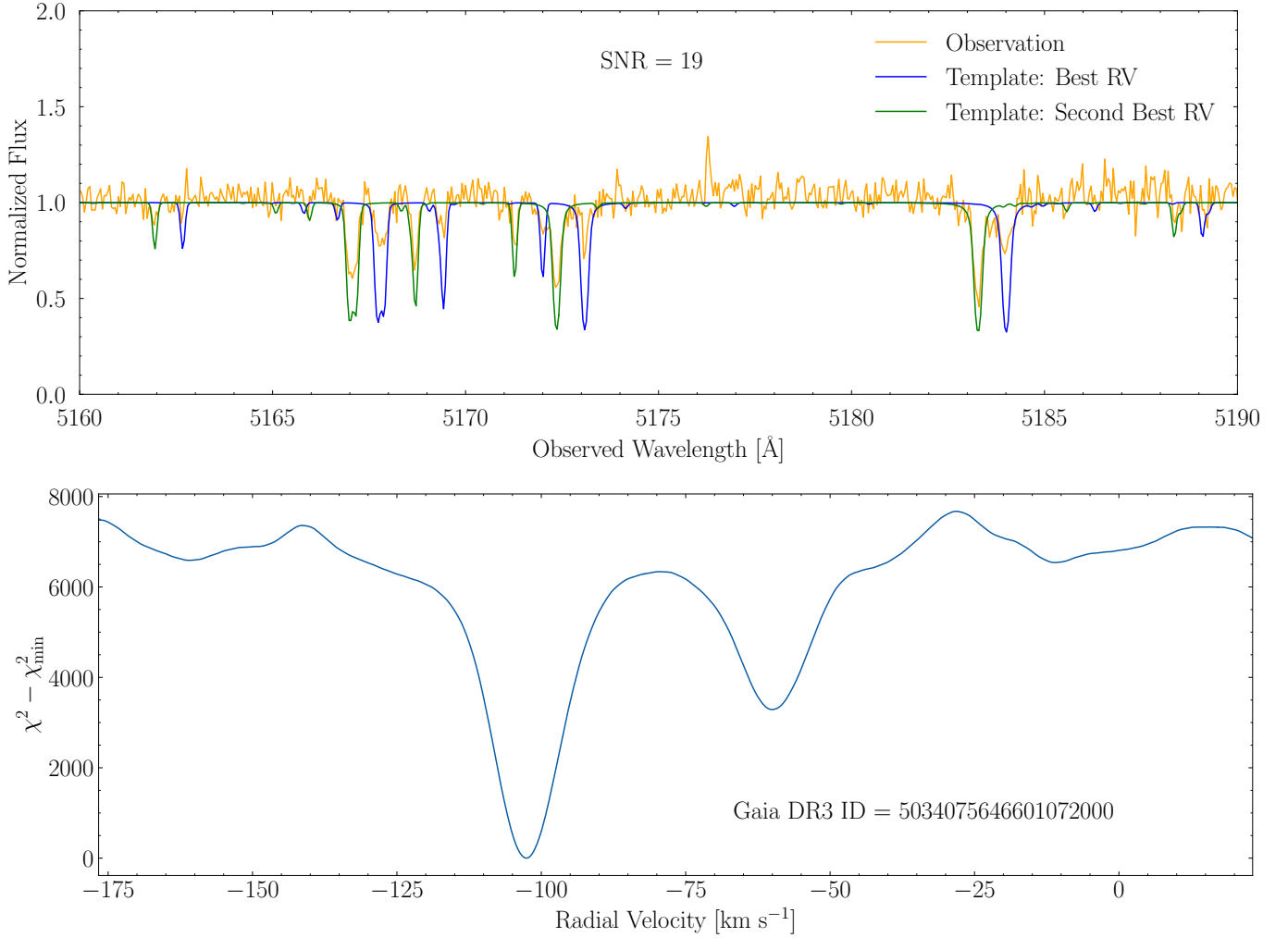


**Figure 5.** Same as Figure 4, but for a target deemed to have a bad template fit. The chi-squared statistic curve is multimodal, suggesting that the system is a double-lined spectroscopic binary (SB2). We show the shifted template spectrum in the lab frame for both plausible RV minima. Lines due to two luminous stars are clearly visible.

tainties are dominated by the uncertainty in the *Gaia* DR3 mean RV, which is often a result of orbital motion rather than the statistical uncertainty on an epoch RV measurement (see Section 6 for further details on the process by which DR3 RVs are computed). As such, we still include the 18 candidates whose largest RV shift is statistically consistent with zero to within  $2\sigma$ , as we do not think that this substantially undermines the evidence indicating the presence of a potential compact object companion.

Of the flagged objects plotted in orange in Figure 6, 52 correspond to low-SNR spectra, while 4 have spectra that are potentially contaminated with moonlight. The remainder were flagged after manual vetting, with 11, 8, and 2 objects determined to be double-lined spectroscopic binaries, hot stars, and fast rotators, respectively. Many of the flagged objects have large RV discrepancies that we find to be spurious, and many of the candidates with large RV discrepancies are flagged. However, sev-

eral genuine candidates survive the vetting process, and are listed in Table 1.

### 5.1. Objects with Multiple RVs

We attempted to obtain at least one additional follow-up RV for each target with  $\text{RV discrepancy} > 10 \text{ km s}^{-1}$ . We plot RVs over time for two typical targets in Table 1 with  $\text{RV discrepancy} > 10 \text{ km s}^{-1}$  in Figure 7. The target in the left panel displays RV variability on short timescales. This suggests that the source is an unresolved hierarchical triple; in this scenario, the observed RV variability arises from the putative inner binary, while the large RUWE value is due to the motion of the outer tertiary. The target in the right panel displays slower RV variability that suggests a long orbital period, consistent with our expectations for typical binaries in our sample.

While the total number of RV epochs per target ranges from 2–20, and we observe some RV variability, we have not yet fully solved the orbit of any of our targets. For

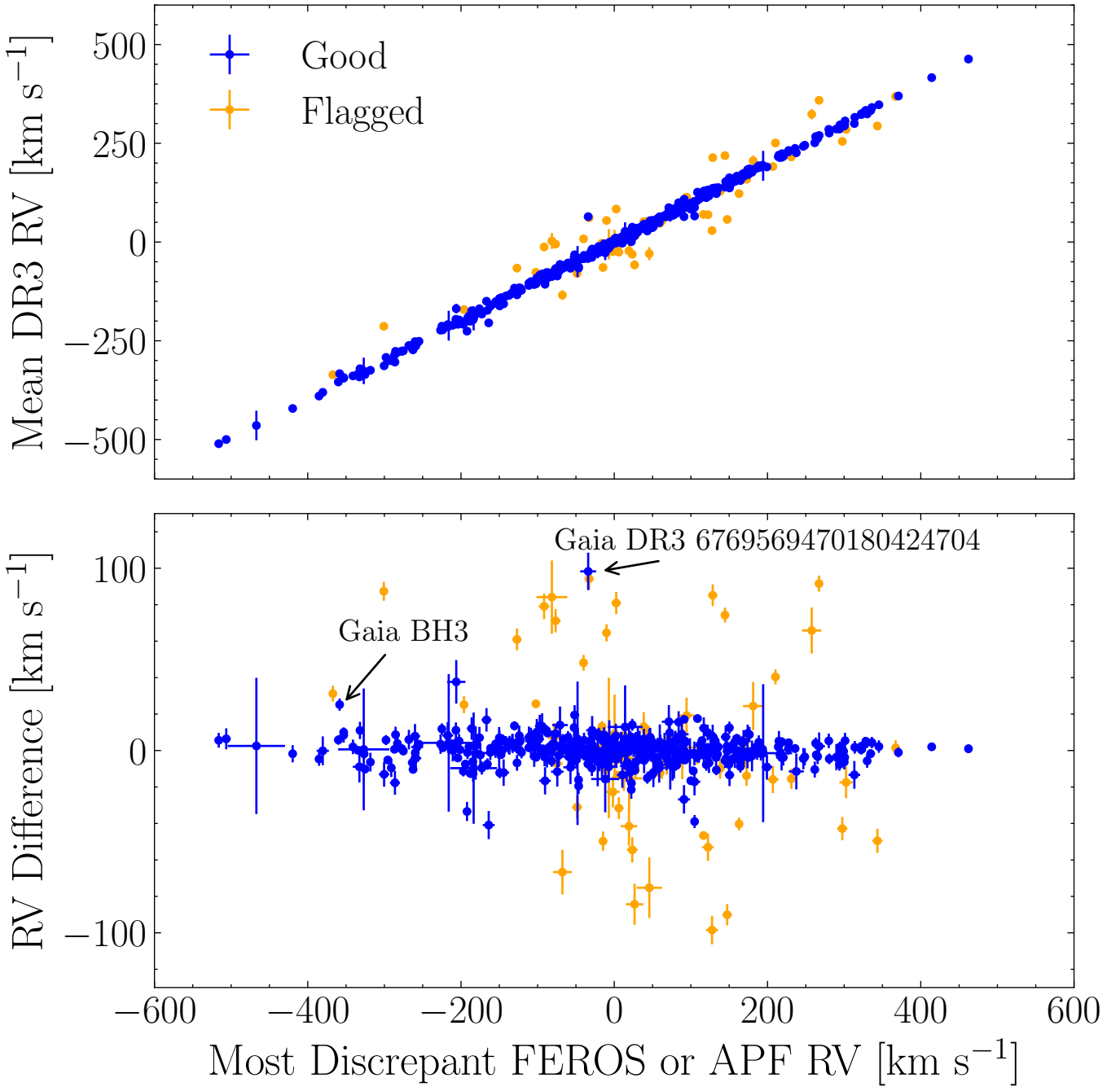


**Figure 6.** Comparison of our derived RVs to the mean RV reported in DR3. RVs for flagged spectra (see Section 4.3) are plotted in orange. In most cases, the RVs are in good agreement. In several cases, the RVs are discrepant, suggesting the presence of a faint or dark companion. We highlight both Gaia BH3 and *Gaia DR3 6769569470180424704*, which has the largest RV discrepancy in our sample.

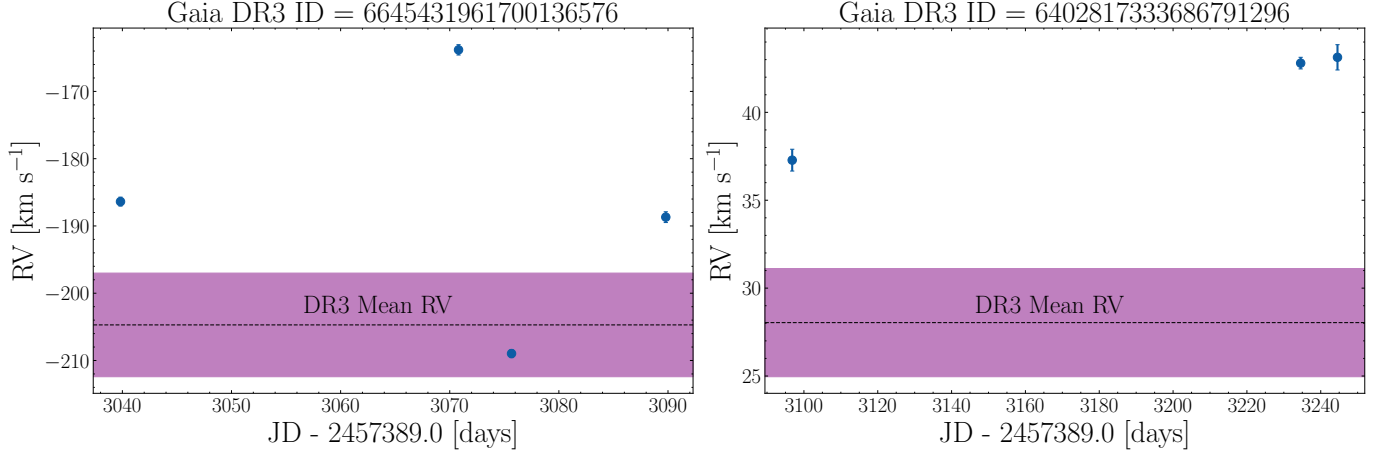


**Figure 7.** Examples of interesting targets with multiple RV measurements. In the left panel, we see RV variability on short timescales, suggesting that the system is potentially a hierarchical triple (see Section 5.1). In the right panel, we see evidence of slower RV variability, but extended RV monitoring is necessary to confirm or rule out a compact object companion.

targets with orbital periods  $\gtrsim 1000$  days, a few RVs taken over a short time frame are insufficient to fit a full orbital solution and tightly constrain the companion mass. Since extended RV monitoring is necessary to determine the orbital period and confirm or rule out a BH or NS companion, we will continue following up in-

teresting candidates over the next several months. Upon release of DR4, we will derive constraints on the companion masses by jointly fitting our long-baseline measurements with epoch *Gaia* astrometry.

**Table 1.** Derived radial velocities (RVs) for all promising candidates with RV difference between epoch RV and mean DR3 RV  $> 10 \text{ km s}^{-1}$ .

<i>Gaia</i> DR3 ID (1)	$N_{\text{RVs, good}}$ (2)	Most Discrepant FEROS or APF RV (3)	<i>Gaia</i> DR3 Mean RV (4)	Largest RV Shift (5)
6769569470180424704	18	$-34.02 \pm 1.62$	$64.26 \pm 10.26$	$98.28 \pm 10.39$
6645431961700136576	4	$-163.82 \pm 0.77$	$-204.71 \pm 7.70$	$40.89 \pm 7.74$
6393888749512565760	2	$104.85 \pm 0.09$	$65.91 \pm 3.57$	$38.94 \pm 3.57$
2123589958955565824	6	$-206.18 \pm 0.33$	$-168.51 \pm 11.93$	$37.67 \pm 11.94$
1109010106866929536	8	$-192.15 \pm 0.38$	$-225.58 \pm 5.24$	$33.43 \pm 5.25$
6714154840051650560	1	$91.02 \pm 0.41$	$64.23 \pm 7.79$	$26.79 \pm 7.80$
4318465066420528000	2	$-358.38 \pm 0.03$	$-333.18 \pm 3.38$	$25.20 \pm 3.38$
5044327218140737536	1	$182.51 \pm 0.65$	$205.68 \pm 13.26$	$23.17 \pm 13.27$
4466423837863123328	3	$-313.02 \pm 0.63$	$-336.00 \pm 4.36$	$22.98 \pm 4.41$
6463410835377385472	2	$22.19 \pm 0.55$	$0.77 \pm 5.02$	$21.42 \pm 5.05$
5817399066319766912	2	$-51.73 \pm 0.92$	$-32.23 \pm 5.38$	$19.50 \pm 5.46$
3190523740098447744	2	$-46.45 \pm 0.05$	$-65.92 \pm 4.26$	$19.47 \pm 4.26$
3252546886080448384	1	$22.43 \pm 0.14$	$4.52 \pm 3.48$	$17.91 \pm 3.48$
1183864824124929792	2	$-286.18 \pm 0.46$	$-303.88 \pm 6.54$	$17.70 \pm 6.56$

**Table 1** *continued*

**Table 1** (*continued*)

<i>Gaia</i> DR3 ID	$N_{\text{RVs, good}}$	Most Discrepant FEROS or APF RV	<i>Gaia</i> DR3 Mean RV	Largest RV Shift
(1)	(2)	km s <sup>-1</sup>	km s <sup>-1</sup>	km s <sup>-1</sup>
		(3)	(4)	(5)
5767212132939510400	3	108.62 ± 0.23	126.17 ± 1.38	17.55 ± 1.40
5470326985368066304	1	104.71 ± 0.72	87.58 ± 7.48	17.13 ± 7.51
2474847090389656064	3	91.26 ± 0.20	108.36 ± 1.61	17.10 ± 1.63
4449971364341398272	3	-166.72 ± 0.42	-149.89 ± 6.44	16.83 ± 6.45
6820303307501354496	1	-90.31 ± 0.78	-106.92 ± 7.46	16.61 ± 7.50
2788486767941706624	3	-229.91 ± 0.53	-213.35 ± 5.21	16.56 ± 5.24
677442515834924416	3	99.91 ± 0.21	83.36 ± 2.10	16.55 ± 2.11
6177352097769902208	2	-46.58 ± 0.26	-62.66 ± 4.00	16.08 ± 4.01
1589175287211605376	1	71.24 ± 0.38	87.06 ± 9.09	15.82 ± 9.10
6822730754297502720	2	-11.79 ± 0.95	-27.42 ± 18.27	15.63 ± 18.30
3529854748080356352	1	84.01 ± 0.05	99.61 ± 5.97	15.60 ± 5.97
3195269030422383488	1	13.74 ± 0.93	29.14 ± 7.83	15.40 ± 7.88
6402817333686791296	3	43.13 ± 0.72	28.04 ± 3.08	15.09 ± 3.16
2402811860245032448	3	23.50 ± 0.03	37.60 ± 3.30	14.10 ± 3.30
2429303635139814400	1	-70.78 ± 0.66	-56.80 ± 10.18	13.98 ± 10.20
1694181735744784768	1	-130.24 ± 0.11	-116.69 ± 2.53	13.55 ± 2.53
2619820000613684992	1	-44.45 ± 0.68	-30.95 ± 6.95	13.50 ± 6.98
5510992972680488832	1	150.43 ± 0.65	136.99 ± 6.07	13.44 ± 6.11
2438001734187492736	2	-97.24 ± 0.18	-83.83 ± 6.20	13.41 ± 6.20
6689320926830067328	1	10.56 ± 0.30	-2.82 ± 7.10	13.38 ± 7.11
6646169837081308032	1	313.32 ± 0.55	299.98 ± 7.59	13.34 ± 7.61
5889520363370193536	1	-94.12 ± 0.44	-80.83 ± 7.11	13.29 ± 7.13
4324114150961924992	2	49.69 ± 0.38	36.46 ± 1.03	13.23 ± 1.10
4036323751356613120	2	-300.32 ± 0.45	-313.37 ± 6.79	13.05 ± 6.81
1445952348525801344	1	14.15 ± 0.08	27.08 ± 22.82	12.93 ± 22.82
1363047492460703744	1	-184.23 ± 0.29	-196.91 ± 4.51	12.68 ± 4.52
1028448477581901184	1	-52.40 ± 0.14	-39.82 ± 4.59	12.58 ± 4.59
4404085239419591552	2	-187.95 ± 0.39	-200.46 ± 2.46	12.51 ± 2.49
6657756868572776832	2	150.28 ± 0.06	162.76 ± 3.37	12.48 ± 3.37
3838404232257203072	1	116.84 ± 0.53	129.14 ± 5.89	12.30 ± 5.91
2281492851046104064	1	-149.54 ± 0.18	-161.73 ± 2.96	12.19 ± 2.96
1805460872350903168	1	-144.36 ± 0.54	-156.45 ± 7.24	12.09 ± 7.26
1911515915671512064	1	-186.06 ± 0.29	-173.99 ± 6.13	12.07 ± 6.14
3619929278952732928	1	51.08 ± 0.69	39.05 ± 8.07	12.03 ± 8.10
4792163228561925504	1	20.64 ± 0.67	8.67 ± 5.15	11.97 ± 5.20
2835800093315146496	2	-224.95 ± 0.23	-213.09 ± 3.03	11.86 ± 3.04

**Table 1** *continued*

**Table 1** (*continued*)

<i>Gaia</i> DR3 ID	$N_{\text{RVs, good}}$	Most Discrepant FEROS or APF RV	<i>Gaia</i> DR3 Mean RV	Largest RV Shift
(1)	(2)	km s <sup>-1</sup>	km s <sup>-1</sup>	km s <sup>-1</sup>
		(3)	(4)	(5)
1343879087778316544	1	$-74.33 \pm 0.27$	$-85.95 \pm 8.14$	$11.62 \pm 8.14$
4344582418904624256	1	$237.59 \pm 0.33$	$226.13 \pm 9.81$	$11.46 \pm 9.82$
4480417902167849728	3	$-196.98 \pm 0.08$	$-208.32 \pm 2.86$	$11.34 \pm 2.87$
5000838062927554176	1	$103.09 \pm 0.24$	$91.90 \pm 2.39$	$11.19 \pm 2.40$
4463022464283196928	1	$-206.62 \pm 0.69$	$-195.49 \pm 4.30$	$11.13 \pm 4.35$
6288565568615343488	1	$-28.83 \pm 0.48$	$-17.72 \pm 7.79$	$11.11 \pm 7.81$
3638399772924914176	1	$-88.54 \pm 0.33$	$-77.50 \pm 2.25$	$11.04 \pm 2.27$
1558668134509319040	2	$-331.81 \pm 0.19$	$-320.78 \pm 4.74$	$11.03 \pm 4.74$
5059047789053289856	1	$26.60 \pm 0.30$	$15.65 \pm 1.78$	$10.95 \pm 1.81$
3270069940330680576	2	$21.49 \pm 0.54$	$10.78 \pm 5.09$	$10.71 \pm 5.12$
5186664770791126912	1	$133.24 \pm 0.36$	$122.56 \pm 2.81$	$10.68 \pm 2.84$
5300091008802250112	1	$261.66 \pm 1.48$	$251.25 \pm 4.40$	$10.41 \pm 4.64$
6903293654893289856	1	$-262.57 \pm 0.07$	$-272.92 \pm 1.17$	$10.35 \pm 1.17$
1115628342232842368	10	$-325.25 \pm 0.06$	$-335.43 \pm 2.27$	$10.18 \pm 2.27$
1698379915953323008	1	$-101.07 \pm 0.29$	$-90.96 \pm 7.24$	$10.11 \pm 7.25$
2292990925172085632	1	$-353.07 \pm 0.15$	$-343.07 \pm 2.66$	$10.00 \pm 2.66$

### 5.2. A Promising Candidate

The target *Gaia* DR3 6769569470180424704 has the largest discrepancy ( $\approx 98$  km s<sup>-1</sup>) between its epoch RV(s) and its *Gaia* DR3 mean RV in Table 1. We obtained several follow-up spectra to investigate the true nature of this object. We present all of our epoch RVs in Figure 8. We find slow acceleration of ( $-11 \pm 2$ ) km s<sup>-1</sup> yr<sup>-1</sup>, with the RV discrepancy growing over time. Extended RV monitoring is warranted.

We obtained a high signal-to-noise spectrum with the Magellan Inamori Kyocera Echelle (MIKE) spectrograph on the Magellan Clay telescope at Las Campanas Observatory (R. Bernstein et al. 2003) on JD 2460480.7435. We used the 0.7" slit with an exposure time of 2700s, yielding spectral resolution  $R \approx 40,000$  over a spectral range of 333–968 nm. The typical SNR per pixel at 5175 Å is  $\approx 70$ . We reduced the spectrum using the MIKE pipeline within CarPy (D. D. Kelson et al. 2000; D. D. Kelson 2003). To combine the orders, we perform an inverse variance-weighted average, and normalize the resulting spectrum using a polynomial spline fit to continuum wavelengths.

Using the approach described by H. Reggiani et al. (2022), we jointly fit the SED and high-resolution spectrum to derive atmospheric parameters for this target. We also measure the equivalent widths of atomic absorp-

tion lines to infer elemental abundances. We provide our best-fit parameters and abundances in Table 2. For comparison, R. Andrae et al. (2023) estimate [Fe/H] = -2.3,  $T_{\text{eff}} = 6200$  K, and  $\log(g/\text{cm s}^{-2}) = 4.2$ . The atmospheric parameters we derive are typical for a low-metallicity halo star (given our selection criteria), and are in reasonable agreement with those provided by R. Andrae et al. (2023). The target's abundance pattern is unremarkable for a low-metallicity halo star. We verify that non-local thermodynamic equilibrium corrections do not strongly affect any of our derived abundances.

We show the position of *Gaia* DR3 6769569470180424704 on an extinction-corrected color-magnitude diagram in the top panel of Figure 9. As before, the extinctions are calculated based on reddenings retrieved from the 3D dust map of G. M. Green et al. (2019). We confirm that the target is bluer than the main sequence of a 100 pc random comparison sample, but has typical colors for a metal-poor halo star.

To check for any signatures of a double-lined spectroscopic binary, we follow the approach of P. Nagarajan et al. (2024a) by comparing the high-resolution MIKE spectrum to objects with similar atmospheric parameters observed by the GALAH survey (S. Buder et al. 2021). Motivated by the derived stellar parameters in Table 1, we retrieve all GALAH spectra with  $T_{\text{eff}} \in (5000, 7000)$  K,  $\log(g/\text{cm s}^{-2}) \in (3.5, 4.5)$ , and

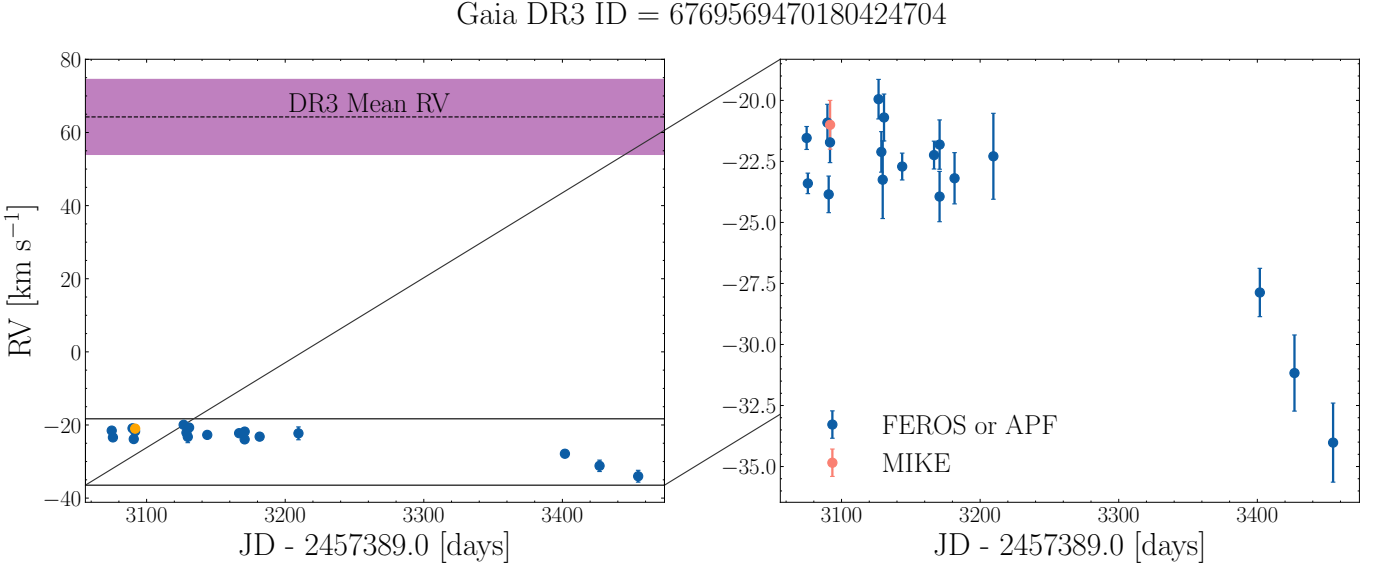


**Figure 8.** RV measurements over time for *Gaia* DR3 6769569470180424704, the target in our sample with the largest discrepancy between its epoch RVs and the mean RV reported in DR3. The instantaneous RVs measured in 2024–2025 differ from the DR3 mean RV in 2014–2017 by more than  $80 \text{ km s}^{-1}$ . The RVs show evidence of acceleration over a time baseline of a few months, but further RV monitoring is necessary to determine the true nature of this compact object candidate.

$[\text{Fe}/\text{H}] < -2.0$ . We then degrade the MIKE spectrum to  $R = 25,000$  and shift all spectra into their respective rest frames. We search for the closest matching GALAH spectra in pixel space by minimizing the total least-squares deviation in the wavelength range of  $(6517 \text{ \AA}, 6690 \text{ \AA})$ . We choose these bounds because virtually all of the signal in the overlapping region between the two spectra arises from the  $\text{H}\alpha$  absorption line. We show the MIKE spectrum along with the closest matching GALAH spectrum in the bottom panel of Figure 9. We do not observe any strong emission lines or other unusual spectral features. The close match rules out the presence of a secondary that makes an appreciable contribution to the total light and has strong  $\text{H}\alpha$  absorption.

Based on the top ten matches in GALAH DR3, we empirically derive stellar parameters of  $T_{\text{eff}} = 6120 \pm 130 \text{ K}$ ,  $\log(g/\text{cm s}^{-2}) = 4.2 \pm 0.2$ ,  $[\text{Fe}/\text{H}] = -2.30 \pm 0.23$ , and  $v_{\text{micro}} = 1.32 \pm 0.07 \text{ km s}^{-1}$  for *Gaia* DR3 6769569470180424704. While hot and metal-poor stars are relatively rare in GALAH DR3, these values are in  $\sim 2\sigma$  agreement with the best-fit derived parameters listed in Table 2.

To summarize, if the *Gaia* DR3 RV is correct, then *Gaia* DR3 6769569470180424704 is very likely to host a dormant BH. However, we do not know if the DR3 RV is accurate, and further monitoring of the acceleration or orbital motion of this target is necessary to determine if this is the case. We check whether plausible orbital solutions that are consistent with the *Gaia* DR3 RV, *Gaia* DR3 RUWE, and epoch RVs exist, following the approach of Müller-Horn et al. (forthcoming). We find that only solutions with large companion masses, long orbital

periods, and high eccentricities are consistent with the observed acceleration, though we defer further analysis of this to future work.

## 6. DISCUSSION

### 6.1. What are the false positives?

False positives in our sample could be targets with spurious *Gaia* DR3 mean RV measurements, or luminous binaries with primary-to-secondary flux ratios high enough to hide the signatures of the faint secondaries. However, we have removed clear double-lined spectroscopic binaries, hot stars, and fast rotators from consideration. While *Gaia*'s RV processing pipeline could still potentially fail to recover the true mean RV for the targets in our vetted sample, it is clear from Figure 6 that the DR3 RVs are reliable for the vast majority of targets.

Luminous hierarchical triples are another possible source of false positives (e.g., D. Bashi & A. Tokovinin 2024). Several objects in Table 1 display RV variability that suggests a short orbital period, with a typical example being the candidate in the left panel of Figure 7. While the large RUWE values for these targets are due to the motion of the outer tertiary, the large RV variability observed on short timescales is due to the orbital motion of the inner binary instead. Indeed, triple systems appear as contaminants whenever a sample of binaries is selected based on both high RUWE and large RV variability (e.g., S. Andrew et al. 2022).

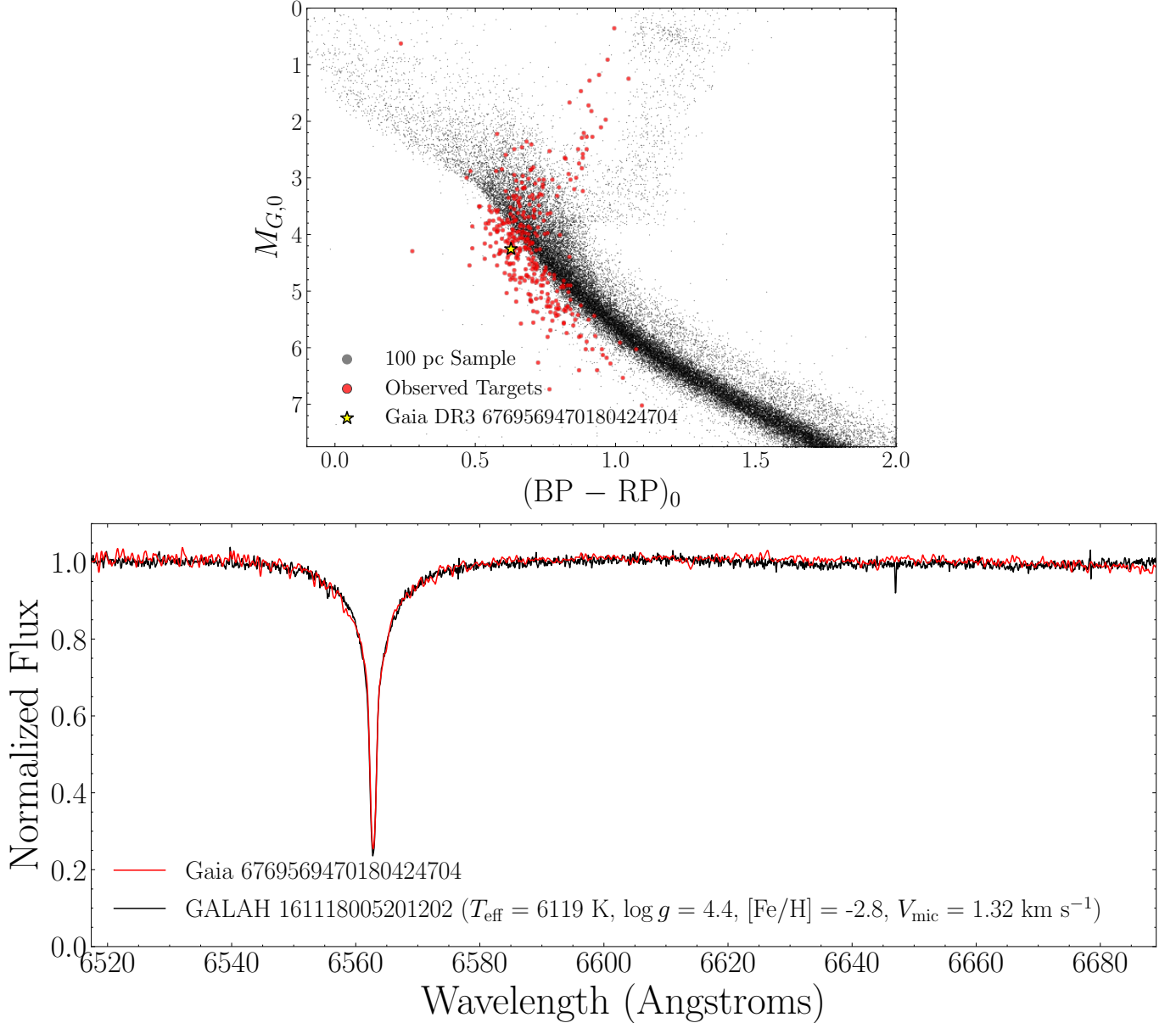


**Figure 9.** Top: Color-magnitude diagram of *Gaia* DR3 6769569470180424704, the BH candidate with the largest RV discrepancy in our observed sample. The target, which is plotted in yellow, is bluer than the main sequence of the 100 pc random comparison sample, but has typical colors for a metal-poor halo star. Bottom: Cutout of a high-resolution optical spectrum of *Gaia* DR3 6769569470180424704 obtained using the MIKE spectrograph; it appears to be a typical  $\sim 0.7 M_{\odot}$  metal-poor main sequence star. The MIKE spectrum of the target is compared against the corresponding region of the spectrum of the object determined to be the closest match in GALAH DR3. The two spectra appear to be quite similar, ruling out the presence of a secondary that makes an appreciable contribution to the total light and has strong H $\alpha$  absorption.

## 6.2. How many low-metallicity stars in our sample have BH companions?

Metal-poor stars in the solar neighborhood are  $\gtrsim 12$  Gyr old (e.g., K. El-Badry et al. 2018; F. Sestito et al. 2021). Using MIST isochrones (J. Choi et al. 2016), we find that metal-poor giants of this age cover a narrow mass range of  $M = (0.78\text{--}0.80) M_{\odot}$ . Assuming a Kroupa IMF (P. Kroupa 2001), there are  $\approx 172$  times

more dwarfs with  $M = (0.1\text{--}0.78) M_{\odot}$  compared to these giants. Assuming that *Gaia* BH3 is the only giant-BH system in our observed sample, and that BH companion probability is independent of luminous star mass in our mass range of interest, how many low-metallicity dwarfs in our sample are likely to have BH companions?

To estimate the answer, we simulate a population of BH + luminous star binaries in the Galactic halo. We draw stars from a Kroupa initial mass function (IMF)

**Table 2.** Stellar parameters and abundances of the red giant in Gaia DR3 6769569470180424704 based on a joint fit of the SED and MIKE spectrum.  $N_{\text{lines}}$  is the number of independent absorption lines used to infer the abundance of each element.

Parameter	Value	$N_{\text{lines}}$
(1)	(2)	(3)
$T_{\text{eff}}$	$6432 \pm 30$ K	
$\log(g/\text{cm s}^{-2})$	$4.42 \pm 0.01$	
[Fe/H]	$-2.29 \pm 0.17$	
$v_{\text{micro}}$	$1.51 \pm 0.19$ km s $^{-1}$	
$t_{\text{age}}$	$13.0 \pm 0.8$ Gyr	
$M_*$	$0.72 \pm 0.01 M_{\odot}$	
$A(\text{Li I})$	2.322	1
[Na I/Fe]	$0.142 \pm 0.068$	2
[Mg I/Fe]	$0.269 \pm 0.096$	7
[Al I/Fe]	$-0.809 \pm 0.111$	2
[Si I/Fe]	$-0.238 \pm 0.059$	1
[Ca I/Fe]	$0.263 \pm 0.039$	12
[Sc II/Fe]	$0.194 \pm 0.090$	12
[Ti I/Fe]	$0.372 \pm 0.055$	5
[Ti II/Fe]	$0.285 \pm 0.061$	27
[Cr II/Fe]	$0.012 \pm 0.090$	3
[Mn I/Fe]	$-0.508 \pm 0.069$	3
[Fe I/H]	$-2.311 \pm 0.045$	74
[Fe II/H]	$-2.289 \pm 0.125$	6
[Co I/Fe]	$0.226 \pm 0.049$	9
[Ni I/Fe]	$-0.013 \pm 0.080$	13
[Sr II/Fe]	$-0.169 \pm 0.104$	2
[Y II/Fe]	$-0.107 \pm 0.076$	3
[Ba II/Fe]	$0.084 \pm 0.028$	1

(P. Kroupa 2001) between 0.1 and  $100 M_{\odot}$ . We sample Galactocentric radii from a power-law distribution, assuming a halo density profile  $\rho(r) \propto r^{-3.5}$  (e.g., X.-X. Xue et al. 2015; C. T. Slater et al. 2016; A. J. Deason et al. 2018; studies that adopt a double power-law profile find a shallower inner slope and steeper outer slope). We then calculate heliocentric distances and retain the stars that lie  $< 2$  kpc away from the Sun, which we place at a distance of 8.122 kpc away from the Galactic Center (GRAVITY Collaboration et al. 2018) and at a height of 20.8 pc above the Galactic mid-plane (M. Bennett & J. Bovy 2019). We estimate absolute magnitudes using synthetic photometry from a 12 Gyr MIST isochrone with initial metallicity [Fe/H] =  $-2.0$ , and use them to

calculate apparent  $G$ -band magnitudes. We draw orbital periods from a log-uniform distribution between 10 and  $10^4$  days (reasonable for Gaia BH3-like systems formed in clusters, see e.g., D. Marín Pina et al. 2024) and eccentricities from a thermal distribution. We assign sky locations by randomly sampling right ascensions and declinations from our catalog of candidate metal-poor binaries. Then, assuming that each luminous star has a  $10 M_{\odot}$  BH companion, we randomly sample binary orientations and calculate DR3 RUWE values using the `gaiamock` code (K. El-Badry et al. 2024). Finally, we apply selection cuts of  $\text{RUWE} > 2.0$  and  $G < 15$  to identify the simulated sources that would make it into our sample. We display the properties of our simulated sample of targets in Figure 10, confirming that brighter and closer binaries tend to have larger predicted RUWE values in DR3.

Based on the location of the Hertzsprung Gap in the color-magnitude diagram in the left panel of Figure 10, we now define giants as stars with absolute  $G$ -band magnitude  $M_{G,0} < 2.5$  and dwarfs as stars with  $M_{G,0} > 2.5$ . We find that there are  $\approx 8$  times more dwarf-BH systems than giant-BH systems in the simulated low-metallicity sample; while the IMF predicts that there are more than 8 dwarfs for every giant, most of those dwarfs are too faint to make it into the sample. Thus, if Gaia BH3 is the only giant-BH system in our observed sample, we expect there to be  $\approx 8$  undiscovered dwarf-BH systems in our observed sample as well. As discussed in Section 6.3 below, we expect our search strategy to recover about half of these compact object binaries.

These predictions depend upon Gaia BH3 being at a “typical” distance ( $d = 0.6$  kpc) for low-metallicity BH binaries, and they could be overestimates if Gaia BH3 is a statistical anomaly. This history of astronomy has witnessed many cases where event rates and space densities based on the first-discovered object were overestimated (e.g., M. Schmidt 1963; B. P. Abbott et al. 2017), so additional low-metallicity BH detections are needed to refine our predictions.

### 6.3. Search sensitivity

To characterize the efficacy of our search, we simulate the fraction of hidden BH companions recovered by our search strategy as a function of orbital period (log-spaced between  $10^2$  and  $10^4$  days) and BH mass (chosen from 5, 10, 20, or  $50 M_{\odot}$ ). We adopt the simulated Galactic population of low-metallicity binaries from Section 6.2. For each binary brighter than  $G < 15$ , we assign sky locations by randomly sampling right ascensions and declinations from our catalog of candidate metal-poor binaries. Then, we randomly sample an eccentricity from a thermal distribution, assign a random binary orientation and phase, and mock observe the binary at a random time.

Using synthetic photometry from the MIST isochrone and Equations 2 and 3 in Gaia Collaboration et al.

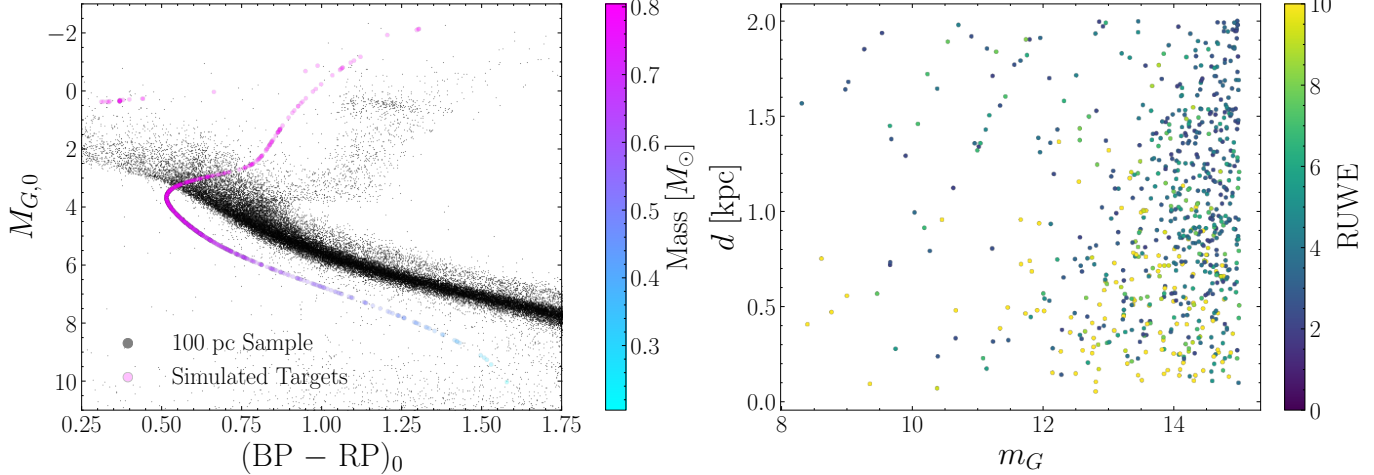


**Figure 10.** Properties of the simulated sample of low-metallicity BH binaries (Section 6.2). Left: Color-magnitude diagram, with a 100 pc random comparison sample shown for reference. The sources are colored by initial mass, and include both dwarfs and giants sampled from a 12 Gyr MIST isochrone with metallicity  $[Fe/H] = -2.0$ . Right: Distance versus apparent magnitude for all simulated targets. The sources are colored by RUWE, with brighter and closer binaries displaying larger excess astrometric noise. We find that  $\approx 8$  dwarfs make it into our sample for every giant.

(2018), we estimate the apparent  $G_{\text{RVS}}$  magnitude of each binary. Then, we simulate a DR3 mean RV for each binary based on the `rv_method_used` parameter in DR3. In detail, for bright stars ( $G_{\text{RVS}} \leq 12$ ), we compute the median of 20 epoch RVs measured over a  $10^3$  d baseline. This is motivated by the fact that the median `rv_nb_transits` in our observed sample is  $\approx 20$ . For fainter stars ( $G_{\text{RVS}} > 12$ ), we instead compute the simulated DR3 RV as the peak of a total cross-correlation function (CCF) constructed from combining 20 individual epoch CCFs. Here, each individual CCF is represented as a Gaussian with a width of  $10 \text{ km s}^{-1}$ . This latter approach approximates the process actually carried out in DR3, implying that the RV reported in DR3 for faint stars is closer to the mode than to the mean of the epoch RVs.

Using `gaiamock`, we compute the fraction of mock observed BH binaries that have both predicted DR3 RUWE  $> 2.0$  and a discrepancy between their epoch RV and mean DR3 RV greater than our adopted threshold of  $10 \text{ km s}^{-1}$ . To derive the uncertainty on this fraction, we repeat our simulation 100 times. We plot our results in Figure 11. We find that, assuming typical orbital periods and BH masses, our search strategy recovers about half of BHs in low-metallicity binaries that lie closer than 2 kpc and have luminous companions brighter than  $G = 15$ . Some real BH binaries may not be recovered if they have orientations close to face-on or are observed at a time during which their epoch RV is similar to their average RV. The search sensitivity peaks at an orbital period of  $\sim 10^3$  d, with the sensitivity being significantly lower at much shorter or longer orbital periods.

The discovery of Gaia BH3 in DR4 pre-release astrometry suggests that luminous companions to Gaia BHs may be dramatically overrepresented at low metallicities. To investigate this hypothesis, we have initiated a radial velocity (RV) survey of metal-poor stars with significant astrometric excess noise (RUWE) values in *Gaia* DR3 using the FEROS and APF spectrographs. We compared these epoch RVs against the mean RV values reported for these targets in DR3 to find potential black hole (BH) and neutron star (NS) candidates. The first results of our survey are reported here; continued monitoring of promising candidates is ongoing. We summarize our main conclusions below.

- *Experimental design:* In Gaia BH3, the red giant’s RV is different from the mean DR3 RV by at least  $20 \text{ km s}^{-1}$  over  $\approx 70\%$  of its orbit, and by at least  $10 \text{ km s}^{-1}$  over  $\approx 85\%$  of its orbit, suggesting that a search strategy for BHs and NSs based on this discrepancy would be effective (Figure 1). Furthermore, for simulated low-metallicity dwarf-BH and giant-BH binaries, the predicted RUWE in DR3 is significantly above a detectability threshold of 2.0 for typical periods of 100–5000 d and distances  $< 2$  kpc (Figure 2). Hence, to search for dormant BHs, we measure instantaneous RVs for low-metallicity stars with elevated RUWE values in DR3 and check whether they are highly discrepant with their corresponding mean DR3 RVs.
- *Summary of the sample:* We select a sample of bright, metal-poor sources with  $[M/H] < -1.0$  and excess astrometric noise in DR3, adopting the robust, data-driven metallicities derived from XP

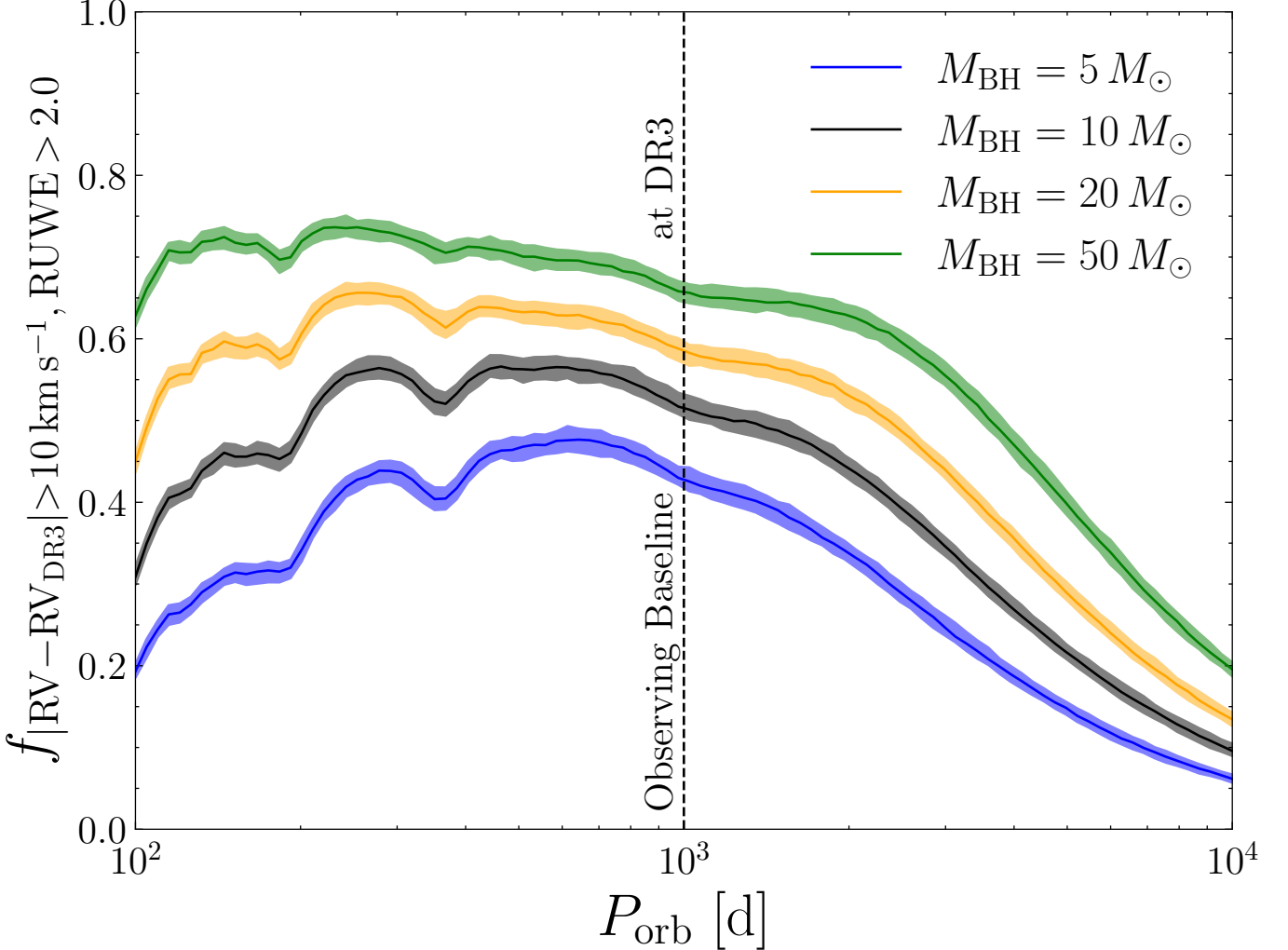


**Figure 11.** Median fraction of BH companions at  $d < 2$  kpc and  $G < 15$  (see Section 6.2) recovered by our search strategy as a function of orbital period and BH mass, with the shaded regions representing a 68% confidence interval. For each binary, we sample eccentricities from a thermal distribution, assign a random orientation and phase, and mock observe the binary at a random time. We simulate their reported mean RVs by approximating the process carried out in DR3 (see Section 6.3). At typical orbital periods and BH masses, we expect to recover at least half of the BHs as candidates, given detection thresholds of an RV discrepancy  $> 10 \text{ km s}^{-1}$  and  $\text{RUWE} > 2.0$ . Some real BH binaries may not be recovered if they have a face-on orientation or are observed at a time during which their epoch RV is similar to their average RV. We find that the search sensitivity peaks at an orbital period of  $\sim 10^3$  d, and is significantly lower at much shorter or longer orbital periods.

spectra by R. Andrae et al. (2023). We use two different selection cuts (Section 3) for targets with  $[\text{M}/\text{H}] < -1.5$  and  $\text{RUWE} > 2.0$  and targets with  $[\text{M}/\text{H}] < -1.0$ ,  $\text{RUWE} > 1.4$ , and large estimated  $a_0$ , respectively. We apply additional quality cuts to exclude marginally resolved binaries and stars with disk-like orbits. We obtained at least one FEROS or APF spectrum for 526 targets out of a sample of 717 candidates, with the remainder scheduled to be observed in the future. The sample of observed targets has  $[\text{M}/\text{H}] < -1.0$ ,  $\text{RUWE} > 1.4$ ,  $G = 9-15$ , and is bluer than the main sequence on a color-magnitude diagram (Figure 3).

- *RV measurements:* We measure epoch RVs by minimizing the chi-squared statistic between the target spectrum and the BOSZ template spectrum with stellar parameters closest to those derived from XP spectra for the target by R. Andrae et al. (2023) (Figure 4). Some spectra have low SNR or are contaminated by moonlight, and others show either a lack of prominent spectral lines or strong evidence of two luminous components (Figure 5). We flag these spectra and remove the corresponding RVs from further consideration. All of our RVs are listed in Table 3.

- *BH/NS candidates:* We compare all of our derived RVs against the mean RVs reported in DR3, finding that most are in good agreement (Figure 6). In several cases, the RVs are discrepant by more than  $10 \text{ km s}^{-1}$ , indicating the potential for a massive, dark companion. We list all promising candidates in Table 1. We obtained additional follow-up spectra for promising targets, but have not yet fully solved the orbits of any candidates (Figure 7). Some targets show short-timescale RV variability, and are likely to be hierarchical triples. Extended RV monitoring will be vital to determine the true nature of these BH or NS candidates.
- *A promising BH candidate:* We identify *Gaia* DR3 676956947018042470 as having the largest discrepancy ( $\approx 98 \text{ km s}^{-1}$ ) between its epoch RVs and its mean RV reported in DR3. We obtained several follow-up spectra, including a high-resolution MIKE spectrum, to investigate this promising BH candidate (Figure 8). From the MIKE spectrum, we infer best-fit stellar parameters and abundances for the target, finding that they are typical for a low-metallicity halo star given our selection criteria (Figure 9). We measure a slow acceleration of  $(-11 \pm 2) \text{ km s}^{-1} \text{ yr}^{-1}$  away from the mean DR3 RV, but without knowledge of whether the reported mean RV is accurate, further monitoring is necessary to determine the candidate's true nature.
- *Simulations:* To characterize the effectiveness of our search strategy, we mock-observe a simulated population of BH + luminous star binaries in the Galactic halo, finding that if *Gaia* BH3 is the only BH + giant binary in our sample, then we expect there to be  $\approx 8$  undiscovered BH + dwarf binaries in our sample as well (Figure 10). We also simulated the fraction of BH companions recovered as a function of orbital period and BH mass, finding that we expect to detect at least half of BH companions with periods of order  $10^3 \text{ d}$  (Figure 11).

We will continue to follow-up the interesting objects identified in Table 1. Since these targets have acceleration solutions or high RUWE values rather than orbital solutions in DR3, the orbital periods of these systems are likely to be on the order of 1–10 years (K. El-Badry et al. 2024). This renders it practically challenging to cover the full RV curves of these targets with spectroscopic follow-up.

However, we will obtain another epoch RV for these targets following the release of DR4, in which many of these objects are likely to receive an orbital solution. This will provide us with at least two RV measurements separated by a multi-year time baseline. We will fit these RVs together with the epoch astrometry in DR4

to constrain the parameters of the low-metallicity binaries with high implied mass functions and uncover any hidden NSs or BHs.

## ACKNOWLEDGMENTS

This research was supported by NSF grant AST-2307232. HWR acknowledges the European Research Council for support from the ERC Advanced Grant ERC-2021-ADG-101054731. CYL acknowledges support from the Harrison and Carnegie Fellowships. This work has made use of data from the European Space Agency (ESA) mission *Gaia* (<https://www.cosmos.esa.int/gaia>), processed by the *Gaia* Data Processing and Analysis Consortium (DPAC, <https://www.cosmos.esa.int/web/gaia/dpac/consortium>). Funding for the DPAC has been provided by national institutions, in particular the institutions participating in the *Gaia* Multilateral Agreement. This paper includes data gathered with the 6.5 meter Magellan Telescopes located at Las Campanas Observatory, Chile.

## AUTHOR CONTRIBUTIONS

PN was responsible for performing the data analysis. KE came up with the initial research concept and obtained the funding. HR measured abundances from the high-resolution spectra. CL, JS, HI, and JL assisted in planning and executing the APF observations, while JMH, RS, HWR, and VC assisted in planning the FEROS observations. JS obtained and reduced the MIKE spectrum. RE measured metallicities from XP spectra. All authors were involved in writing and editing the manuscript.

*Facilities:* APF, Max Planck:2.2m (FEROS), Magellan:Baade (MIKE)

*Software:* astropy (Astropy Collaboration et al. 2013, 2018, 2022)

## APPENDIX

## A. RADIAL VELOCITIES

We provide a summary of all of our measured radial velocities (RVs) in Table 3. We group RVs by target and sort by largest RV discrepancy with the mean RV reported in DR3. We flag unreliable RVs derived from

spectra that have either low signal-to-noise (SNR) values  $< 2$  at 5200 Å or moonlight contamination that causes the barycenter correction (BC) to be within  $10 \text{ km s}^{-1}$  of the derived RV. We also flag RVs derived from spectra visually identified to be of hot stars (hot), fast rotators ( $v \sin i$ ), or spectroscopic binaries (SB2).

**Table 3.** Derived radial velocities (RVs) for all observed targets. We also provide the mean RV reported in *Gaia* DR3 for comparison.

<i>Gaia</i> DR3 ID (1)	JD d (2)	RV km s <sup>-1</sup> (3)	<i>Gaia</i> DR3 Mean RV km s <sup>-1</sup> (4)	Flags (5)	RV Shift km s <sup>-1</sup> (6)
			(4)		
31530905403904512	2460559.9042	$-59.67 \pm 0.11$	$-58.95 \pm 1.94$		$0.72 \pm 1.95$
31530905403904512	2460570.8191	$-65.16 \pm 0.14$	$-58.95 \pm 1.94$		$6.21 \pm 1.95$
75519548132523136	2460569.8113	$58.07 \pm 0.20$	$50.99 \pm 4.27$		$7.08 \pm 4.28$
187869776566408960	2460575.8128	$25.09 \pm 0.24$	$27.81 \pm 6.21$		$2.72 \pm 6.21$
207547530009853952	2460574.8033	$11.79 \pm 0.26$	$13.02 \pm 3.99$		$1.23 \pm 4.00$
249249188555702784	2460563.9349	$-285.39 \pm 0.19$	$-276.70 \pm 4.36$		$8.69 \pm 4.36$
290511523477577600	2460553.9909	$-48.02 \pm 0.17$	$-41.60 \pm 3.33$		$6.42 \pm 3.34$
316060462855379840	2460566.8837	$-216.74 \pm 0.20$	$-214.23 \pm 3.83$		$2.51 \pm 3.84$
316671516442699520	2460563.9599	$-29.18 \pm 0.29$	$-38.81 \pm 4.38$		$9.63 \pm 4.39$
327354611937489024	2460563.9116	$30.82 \pm 0.21$	$35.45 \pm 7.80$		$4.63 \pm 7.80$
363631486266516992	2460568.7686	$-20.05 \pm 0.14$	$-22.66 \pm 4.68$		$2.61 \pm 4.68$
374072654842343040	2460555.8470	$-121.06 \pm 0.21$	$-122.09 \pm 3.28$		$1.03 \pm 3.29$
402635355594132224	2460550.9485	$-259.61 \pm 0.16$	$-260.76 \pm 3.00$		$1.15 \pm 3.00$
462765992951416064	2460562.7899	$49.62 \pm 0.12$	$48.33 \pm 2.70$	BC	$1.29 \pm 2.70$
524686025365395328	2460547.9620	$-67.66 \pm 0.57$	$-134.35 \pm 12.26$	hot	$66.69 \pm 12.27$
583416851271964544	2460448.4926	$174.86 \pm 0.20$	$170.99 \pm 1.78$		$3.87 \pm 1.79$
589980763891303040	2460448.5106	$68.35 \pm 0.62$	$64.24 \pm 6.74$		$4.11 \pm 6.77$
596344015638431104	2460738.6926	$62.25 \pm 1.19$	$54.30 \pm 7.57$	SNR	$7.95 \pm 7.66$
614970803468896640	2460428.5437	$-10.51 \pm 0.12$	$-9.61 \pm 3.75$		$0.90 \pm 3.75$
619887407151659648	2460450.4587	$79.65 \pm 0.20$	$78.99 \pm 1.77$		$0.66 \pm 1.78$
654976435263115520	2460737.6410	$147.39 \pm 1.07$	$57.29 \pm 5.85$	SNR	$90.10 \pm 5.95$
659538102848458112	2460424.4863	$-52.14 \pm 0.62$	$-49.62 \pm 6.17$		$2.52 \pm 6.20$
677442515834924416	2460587.0107	$72.00 \pm 0.09$	$83.36 \pm 2.10$		$11.36 \pm 2.10$
677442515834924416	2460728.8677	$99.91 \pm 0.21$	$83.36 \pm 2.10$		$16.55 \pm 2.11$
677442515834924416	2460760.7451	$90.48 \pm 0.26$	$83.36 \pm 2.10$		$7.12 \pm 2.12$
719669191180911488	2460587.0275	$114.40 \pm 0.02$	$119.84 \pm 1.88$		$5.44 \pm 1.88$

**Table 3** *continued*

**Table 3** (*continued*)

<i>Gaia</i> DR3 ID	JD d	RV km s <sup>-1</sup>	<i>Gaia</i> DR3 Mean RV	Flags	RV Shift km s <sup>-1</sup>
			(4)		
(1)	(2)	(3)		(5)	(6)
85958402366008320	2460824.7779	-141.46 ± 0.24	-136.69 ± 3.16		4.77 ± 3.17
866004705550987264	2460577.9367	302.54 ± 0.66	285.06 ± 8.71	SB2	17.48 ± 8.74
874790215772404608	2460577.9583	62.87 ± 0.11	63.07 ± 1.54		0.20 ± 1.55
890970938125057280	2460580.9244	131.73 ± 0.24	135.98 ± 5.02		4.25 ± 5.02
900812185667820160	2460581.9443	162.62 ± 0.20	157.72 ± 3.26		4.90 ± 3.26
979611641410430336	2460580.9015	-2.09 ± 0.20	2.82 ± 3.19		4.91 ± 3.19
988342141692595328	2460577.9785	2.02 ± 0.26	10.08 ± 6.67		8.06 ± 6.68
1028448477581901184	2460586.0190	-52.40 ± 0.14	-39.82 ± 4.59		12.58 ± 4.59
1028448477581901184	2460717.8399	-31.67 ± 0.20	-39.82 ± 4.59	BC	8.15 ± 4.60
1028448477581901184	2460728.8023	-34.53 ± 0.17	-39.82 ± 4.59	BC	5.29 ± 4.59
1028448477581901184	2460760.7307	-41.74 ± 0.21	-39.82 ± 4.59	BC	1.92 ± 4.60
1030880524287375360	2460585.9656	25.74 ± 0.06	32.16 ± 2.11		6.42 ± 2.11
1052266579499163392	2460581.9223	-180.84 ± 0.21	-182.21 ± 14.62		1.37 ± 14.62
1073062536268418688	2460581.9032	-103.49 ± 0.38	-101.68 ± 3.33		1.81 ± 3.35
1087217545885449600	2460573.8435	41.41 ± 0.18	51.92 ± 2.01	BC	10.51 ± 2.01
1093810767362290560	2460566.9202	-57.74 ± 0.20	-57.87 ± 2.41		0.13 ± 2.42
1095232470257179264	2460575.8412	-286.81 ± 0.19	-286.13 ± 1.45		0.68 ± 1.46
1109010106866929536	2460566.9042	-239.55 ± 0.21	-225.58 ± 5.24		13.97 ± 5.24
1109010106866929536	2460582.7266	-197.66 ± 0.26	-225.58 ± 5.24		27.92 ± 5.24
1109010106866929536	2460582.7412	-198.14 ± 0.29	-225.58 ± 5.24		27.44 ± 5.25
1109010106866929536	2460584.7458	-192.23 ± 0.35	-225.58 ± 5.24		33.35 ± 5.25
1109010106866929536	2460584.7602	-192.15 ± 0.38	-225.58 ± 5.24		33.43 ± 5.25
1109010106866929536	2460584.7743	-192.16 ± 0.44	-225.58 ± 5.24		33.42 ± 5.26
1109010106866929536	2460586.7461	-207.77 ± 0.32	-225.58 ± 5.24		17.81 ± 5.25
1109010106866929536	2460586.7554	-207.99 ± 0.62	-225.58 ± 5.24		17.59 ± 5.28
1115628342232842368	2460562.7526	-338.01 ± 0.06	-335.43 ± 2.27		2.58 ± 2.27
1115628342232842368	2460704.6419	-325.35 ± 0.06	-335.43 ± 2.27		10.08 ± 2.27
1115628342232842368	2460704.6564	-325.35 ± 0.07	-335.43 ± 2.27		10.08 ± 2.27
1115628342232842368	2460704.6715	-325.25 ± 0.06	-335.43 ± 2.27		10.18 ± 2.27
1115628342232842368	2460716.8832	-344.32 ± 0.09	-335.43 ± 2.27		8.89 ± 2.27
1115628342232842368	2460716.8975	-344.67 ± 0.09	-335.43 ± 2.27		9.24 ± 2.27
1115628342232842368	2460716.9124	-344.40 ± 0.07	-335.43 ± 2.27		8.97 ± 2.27
1115628342232842368	2460716.9267	-344.49 ± 0.07	-335.43 ± 2.27		9.06 ± 2.27
1115628342232842368	2460728.8503	-325.58 ± 0.09	-335.43 ± 2.27		9.85 ± 2.27
1115628342232842368	2460735.9621	-333.13 ± 0.06	-335.43 ± 2.27		2.30 ± 2.27
1126103148991284352	2460560.7631	-353.07 ± 0.22	-344.65 ± 4.07		8.42 ± 4.07

**Table 3** *continued*

**Table 3** (*continued*)

<i>Gaia</i> DR3 ID	JD	RV	<i>Gaia</i> DR3 Mean RV	Flags	RV Shift
	d	km s <sup>-1</sup>	km s <sup>-1</sup>		km s <sup>-1</sup>
(1)	(2)	(3)	(4)	(5)	(6)
1141203188852721664	2460562.7343	14.78 ± 0.30	21.32 ± 3.53		6.54 ± 3.55
1149756736482072576	2460537.7687	-122.94 ± 0.21	-123.01 ± 2.73		0.07 ± 2.74
1161094075752619136	2460424.7526	-74.92 ± 0.47	-82.03 ± 7.31	SB2	7.11 ± 7.32
1161094075752619136	2460481.6773	-77.98 ± 0.74	-82.03 ± 7.31	SB2	4.05 ± 7.35
1177824863156087296	2460479.6275	-111.35 ± 0.66	-104.18 ± 6.01		7.17 ± 6.05
1183864824124929792	2460485.6361	-286.18 ± 0.46	-303.88 ± 6.54		17.70 ± 6.56
1183864824124929792	2460738.7903	-310.87 ± 1.33	-303.88 ± 6.54		6.99 ± 6.68
1186550724873052160	2460481.5755	-27.25 ± 0.17	-30.58 ± 1.88		3.33 ± 1.88
1196101907506720000	2460480.6215	34.81 ± 0.33	36.82 ± 6.21		2.01 ± 6.22
1232281475056475392	2460478.5826	83.55 ± 0.53	83.16 ± 2.68		0.39 ± 2.73
1236373685536404096	2460515.4817	-80.89 ± 0.56	-77.47 ± 7.49		3.42 ± 7.51
1246628349452501120	2460740.7890	2.59 ± 0.12	83.53 ± 6.08	SNR	80.94 ± 6.08
1255225155992171392	2460813.7746	1.89 ± 0.13	4.97 ± 2.64		3.08 ± 2.64
1281359310434033664	2460806.8174	-147.77 ± 0.29	-150.04 ± 2.15		2.27 ± 2.17
1283083482105602560	2460813.8110	-107.95 ± 0.21	-105.40 ± 1.57		2.55 ± 1.59
1284896817297504896	2460801.8186	-126.88 ± 0.47	-133.63 ± 4.32		6.75 ± 4.35
1290088711204610560	2460825.8357	-0.75 ± 0.24	0.54 ± 2.44		1.29 ± 2.45
1319379563529749120	2460817.8264	-165.54 ± 0.35	-172.99 ± 3.12		7.45 ± 3.14
1324064475199832448	2460582.7102	-194.23 ± 0.11	-201.67 ± 1.07		7.44 ± 1.08
1343879087778316544	2460535.7197	-74.33 ± 0.27	-85.95 ± 8.14		11.62 ± 8.14
1360311082896731136	2460573.7517	-260.03 ± 0.42	-252.14 ± 6.64		7.89 ± 6.65
1363047492460703744	2460542.7441	-184.23 ± 0.29	-196.91 ± 4.51		12.68 ± 4.52
1373410286472677888	2460819.7913	-72.37 ± 0.24	-75.04 ± 6.34		2.67 ± 6.34
1394552589404881152	2460813.8255	-127.01 ± 0.54	-125.63 ± 2.91		1.38 ± 2.96
1397583290127619840	2460583.7263	-149.62 ± 0.21	-145.13 ± 2.73		4.49 ± 2.74
1419359598952013952	2460543.7390	-282.91 ± 0.21	-279.07 ± 3.65		3.84 ± 3.66
1422064500635586688	2460531.7299	-205.12 ± 0.08	-201.03 ± 3.32		4.09 ± 3.32
1445952348525801344	2460815.7786	14.15 ± 0.08	27.08 ± 22.82		12.93 ± 22.82
1475027838306979200	2460828.7687	48.52 ± 0.11	54.04 ± 2.02		5.52 ± 2.02
1479535389306190976	2460473.7443	-34.36 ± 0.56	-35.78 ± 1.34	BC	1.42 ± 1.45
1479535389306190976	2460818.8051	-36.25 ± 0.11	-35.78 ± 1.34	BC	0.47 ± 1.34
1481189192231609472	2460820.8115	-133.15 ± 0.21	-128.98 ± 4.91		4.17 ± 4.92
1489161373086670848	2460820.7600	-174.77 ± 0.27	-177.21 ± 5.55		2.44 ± 5.55
1489688863790805376	2460818.7585	-124.05 ± 0.18	-119.57 ± 4.40		4.48 ± 4.40
1497188495164830592	2460818.7846	-20.20 ± 0.20	-11.31 ± 3.60		8.89 ± 3.61
1510085903997844864	2460797.8060	-57.79 ± 0.44	-55.20 ± 7.00		2.59 ± 7.02

**Table 3** *continued*

**Table 3** (*continued*)

<i>Gaia</i> DR3 ID	JD	RV	<i>Gaia</i> DR3 Mean RV	Flags	RV Shift
	d	km s <sup>-1</sup>	km s <sup>-1</sup>		km s <sup>-1</sup>
(1)	(2)	(3)	(4)	(5)	(6)
1512383367903955840	2460811.7790	-104.30 ± 0.39	-102.86 ± 5.20		1.44 ± 5.22
1527759075945701376	2460829.7525	-1.84 ± 0.26	-1.85 ± 3.21		0.01 ± 3.22
1542487652676277760	2460829.7880	-226.66 ± 0.32	-223.12 ± 5.38		3.54 ± 5.39
1558668134509319040	2460807.7762	-328.65 ± 0.78	-320.78 ± 4.74		7.87 ± 4.80
1558668134509319040	2460811.7571	-331.81 ± 0.19	-320.78 ± 4.74		11.03 ± 4.74
1570143840447017984	2460786.7921	-67.77 ± 0.15	-67.17 ± 2.19		0.60 ± 2.19
1574040337856735616	2460820.7839	-175.95 ± 0.68	-168.91 ± 5.92		7.04 ± 5.96
1589175287211605376	2460806.8404	71.24 ± 0.38	87.06 ± 9.09		15.82 ± 9.10
1598550960300560896	2460568.7448	19.33 ± 0.29	25.77 ± 6.22		6.44 ± 6.22
1625301043116465536	2460538.7154	-20.29 ± 0.09	-19.94 ± 3.12	BC	0.35 ± 3.12
1650922176599904000	2460486.7830	-465.94 ± 0.22	-464.48 ± 37.37		1.46 ± 37.37
1650922176599904000	2460533.7698	-467.00 ± 0.12	-464.48 ± 37.37		2.52 ± 37.37
1657453619266736512	2460804.8068	8.76 ± 0.36	11.65 ± 7.22		2.89 ± 7.23
1663937336255868032	2460786.8118	-258.93 ± 0.24	-263.13 ± 7.07		4.20 ± 7.08
1685539544286096384	2460561.7649	21.28 ± 0.21	25.11 ± 6.70		3.83 ± 6.71
1694181735744784768	2460543.7584	-130.24 ± 0.11	-116.69 ± 2.53		13.55 ± 2.53
1698379915953323008	2460561.7148	-101.07 ± 0.29	-90.96 ± 7.24		10.11 ± 7.25
1711902775103746560	2460543.7739	-275.23 ± 0.16	-275.50 ± 2.19		0.27 ± 2.20
1723726369097005312	2460529.7376	-295.51 ± 0.15	-300.69 ± 1.87		5.18 ± 1.88
1731732737892580352	2460464.8922	-29.07 ± 0.03	-19.62 ± 1.59		9.45 ± 1.59
1779469856283608064	2460509.7781	-149.97 ± 0.18	-143.04 ± 4.00		6.93 ± 4.00
1788672665525489920	2460622.5354	-28.63 ± 0.47	-25.56 ± 2.24		3.07 ± 2.29
1805460872350903168	2460480.8230	-144.36 ± 0.54	-156.45 ± 7.24		12.09 ± 7.26
1810297692736381184	2460460.8604	-204.10 ± 0.20	-208.18 ± 1.83		4.08 ± 1.84
1840445472621264896	2460535.7920	-216.00 ± 0.09	-211.78 ± 37.73		4.22 ± 37.73
1843327159458210816	2460525.8416	-86.93 ± 0.08	-77.35 ± 1.63		9.58 ± 1.64
1880593731688347264	2460526.8949	-277.52 ± 0.06	-276.46 ± 1.80		1.06 ± 1.81
1908577986244357632	2460548.7804	-59.92 ± 0.03	-59.60 ± 3.50		0.32 ± 3.50
1911515915671512064	2460551.8352	-186.06 ± 0.29	-173.99 ± 6.13		12.07 ± 6.14
1919029703259598336	2460555.8084	-108.30 ± 0.36	-101.42 ± 4.40		6.88 ± 4.41
1940380874743387776	2460544.8901	-326.90 ± 0.09	-326.27 ± 33.44		0.63 ± 33.44
1974994776399961216	2460541.7816	-67.40 ± 0.27	-64.76 ± 6.39		2.64 ± 6.40
1976290172899067264	2460526.8769	-133.67 ± 0.17	-129.48 ± 3.11		4.19 ± 3.12
1985939452581432320	2460541.8157	-23.47 ± 0.12	-23.48 ± 3.00		0.01 ± 3.00
2012367039189084928	2460498.7167	-108.28 ± 0.08	-100.10 ± 1.78		8.18 ± 1.79
2012367039189084928	2460541.0222	-108.55 ± 0.03	-100.10 ± 1.78		8.45 ± 1.78

**Table 3** *continued*

**Table 3** (*continued*)

<i>Gaia</i> DR3 ID	JD	RV	<i>Gaia</i> DR3 Mean RV	Flags	RV Shift
	d	km s <sup>-1</sup>	km s <sup>-1</sup>		km s <sup>-1</sup>
(1)	(2)	(3)	(4)	(5)	(6)
2012367039189084928	2460541.7998	$-108.42 \pm 0.03$	$-100.10 \pm 1.78$		$8.32 \pm 1.78$
2038568298219233152	2460528.7766	$-297.82 \pm 0.25$	$-292.08 \pm 2.75$		$5.74 \pm 2.76$
2046121840007606144	2460531.7873	$-64.99 \pm 0.17$	$-63.85 \pm 2.81$		$1.14 \pm 2.81$
2047697989948528640	2460542.7809	$-360.04 \pm 0.03$	$-354.24 \pm 2.61$		$5.80 \pm 2.61$
2054522692957346944	2460529.7828	$-108.15 \pm 0.12$	$-104.85 \pm 1.53$		$3.30 \pm 1.53$
2074915468249960448	2460536.7596	$-217.32 \pm 0.12$	$-209.04 \pm 7.29$		$8.28 \pm 7.29$
2075888368550754048	2460531.7708	$-42.20 \pm 0.20$	$-41.57 \pm 3.38$		$0.63 \pm 3.39$
2096216586192095360	2460548.7354	$-49.11 \pm 0.41$	$-54.05 \pm 4.95$		$4.94 \pm 4.96$
2107991153134598144	2460561.7451	$-81.64 \pm 0.14$	$-87.39 \pm 3.16$		$5.75 \pm 3.16$
2118002687540997504	2460537.7302	$-332.59 \pm 0.25$	$-341.50 \pm 8.61$		$8.91 \pm 8.61$
2119880309803249664	2460532.7342	$-516.14 \pm 0.33$	$-510.52 \pm 4.04$		$5.62 \pm 4.06$
2123589958955565824	2460535.7718	$-190.53 \pm 0.20$	$-168.51 \pm 11.93$		$22.02 \pm 11.94$
2123589958955565824	2460587.6801	$-166.31 \pm 0.24$	$-168.51 \pm 11.93$		$2.20 \pm 11.94$
2123589958955565824	2460733.9132	$-191.92 \pm 0.33$	$-168.51 \pm 11.93$		$23.41 \pm 11.94$
2123589958955565824	2460788.9790	$-206.18 \pm 0.33$	$-168.51 \pm 11.93$		$37.67 \pm 11.94$
2123589958955565824	2460801.9420	$-194.14 \pm 0.44$	$-168.51 \pm 11.93$		$25.63 \pm 11.94$
2123589958955565824	2460828.9601	$-146.62 \pm 0.23$	$-168.51 \pm 11.93$		$21.89 \pm 11.94$
2178042207182395008	2460533.7984	$-318.24 \pm 0.25$	$-324.61 \pm 5.11$		$6.37 \pm 5.12$
2230058934051637760	2460526.9145	$-39.41 \pm 0.32$	$-33.77 \pm 4.12$		$5.64 \pm 4.13$
2236448775937348352	2460525.8244	$-257.22 \pm 0.24$	$-255.30 \pm 7.74$		$1.92 \pm 7.75$
2256036476802548608	2460529.7530	$-189.61 \pm 0.03$	$-187.59 \pm 1.72$		$2.02 \pm 1.72$
2281492851046104064	2460527.9022	$-149.54 \pm 0.18$	$-161.73 \pm 2.96$		$12.19 \pm 2.96$
2292990925172085632	2460528.7569	$-353.07 \pm 0.15$	$-343.07 \pm 2.66$		$10.00 \pm 2.66$
2306397751485602944	2460517.8670	$-16.01 \pm 0.83$	$-23.54 \pm 7.28$		$7.53 \pm 7.33$
2306554049640181760	2460517.8837	$8.70 \pm 0.58$	$7.05 \pm 5.71$		$1.65 \pm 5.74$
2315687662667389184	2460600.6788	$38.99 \pm 0.32$	$33.55 \pm 6.98$		$5.44 \pm 6.98$
2332061310654863360	2460479.9237	$92.20 \pm 0.06$	$87.01 \pm 2.11$		$5.19 \pm 2.12$
2344504075725183104	2460519.8773	$-76.59 \pm 0.12$	$-73.71 \pm 2.27$		$2.88 \pm 2.27$
2379115460522368640	2460623.6257	$-104.42 \pm 0.26$	$-107.57 \pm 5.80$		$3.15 \pm 5.80$
2400926678839820800	2460517.7812	$-94.07 \pm 0.08$	$-94.85 \pm 2.62$		$0.78 \pm 2.63$
2402811860245032448	2460481.9391	$27.55 \pm 0.02$	$37.60 \pm 3.30$		$10.05 \pm 3.30$
2402811860245032448	2460629.5739	$23.50 \pm 0.03$	$37.60 \pm 3.30$		$14.10 \pm 3.30$
2402811860245032448	2460633.5548	$23.74 \pm 0.03$	$37.60 \pm 3.30$		$13.86 \pm 3.30$
2409013453718653824	2460624.6115	$18.60 \pm 0.34$	$22.80 \pm 3.88$		$4.20 \pm 3.89$
2410710034520071808	2460517.7977	$-124.54 \pm 0.33$	$-119.17 \pm 6.17$		$5.37 \pm 6.18$
2429303635139814400	2460629.6413	$-70.78 \pm 0.66$	$-56.80 \pm 10.18$		$13.98 \pm 10.20$

**Table 3** *continued*

**Table 3** (*continued*)

<i>Gaia</i> DR3 ID	JD d	RV km s <sup>-1</sup>	<i>Gaia</i> DR3 Mean RV	Flags	RV Shift km s <sup>-1</sup>
			(4)		
(1)	(2)	(3)	(4)	(5)	(6)
2438001734187492736	2460519.8280	-97.24 ± 0.18	-83.83 ± 6.20		13.41 ± 6.20
2438001734187492736	2460560.6855	-86.26 ± 0.20	-83.83 ± 6.20		2.43 ± 6.20
2438414532084246528	2460518.8925	-56.97 ± 0.39	-55.77 ± 5.69		1.20 ± 5.70
2474847090389656064	2460568.8389	91.26 ± 0.20	108.36 ± 1.61		17.10 ± 1.63
2474847090389656064	2460574.7516	91.41 ± 0.23	108.36 ± 1.61		16.95 ± 1.63
2474847090389656064	2460597.6945	92.40 ± 0.15	108.36 ± 1.61		15.96 ± 1.62
2482621256072699904	2460575.8227	-385.23 ± 0.46	-389.88 ± 3.71		4.65 ± 3.74
2487686225105416320	2460621.5824	-57.12 ± 0.77	-66.31 ± 9.19		9.19 ± 9.23
2492878703127223424	2460569.7471	56.46 ± 0.51	59.25 ± 4.14		2.79 ± 4.17
2511840193465032448	2460598.7108	9.43 ± 0.29	12.41 ± 7.32		2.98 ± 7.33
2524030925559608448	2460519.8610	-51.47 ± 0.14	-52.79 ± 1.72		1.32 ± 1.72
2554217295745049856	2460519.8444	-145.80 ± 0.48	-145.50 ± 2.04		0.30 ± 2.10
2566537942009510528	2460568.8061	-59.41 ± 0.15	-59.14 ± 3.15		0.27 ± 3.16
2570244979822205696	2460568.8228	-35.34 ± 0.08	-36.18 ± 1.99		0.84 ± 1.99
2589877859447847424	2460580.7619	-136.73 ± 0.83	-133.85 ± 5.13		2.88 ± 5.20
2613006872517192960	2460517.7564	-137.72 ± 0.87	-135.14 ± 4.30		2.58 ± 4.38
2613006872517192960	2460577.7052	-137.30 ± 0.54	-135.14 ± 4.30		2.16 ± 4.33
2613006872517192960	2460577.7682	-136.31 ± 0.74	-135.14 ± 4.30		1.17 ± 4.36
2618223166132715776	2460627.5910	-76.37 ± 0.48	-67.11 ± 4.79		9.26 ± 4.82
2619117515762724352	2460628.5762	65.59 ± 0.48	67.05 ± 8.21		1.46 ± 8.22
2619820000613684992	2460561.7327	23.53 ± 0.23	-30.95 ± 6.95	SNR	54.48 ± 6.95
2619820000613684992	2460628.5515	-44.45 ± 0.68	-30.95 ± 6.95		13.50 ± 6.98
2643383531229432320	2460510.8555	-47.90 ± 0.06	-49.40 ± 39.34		1.50 ± 39.34
2645540051488656768	2460624.5877	19.79 ± 0.88	14.34 ± 8.30	SNR	5.45 ± 8.35
2667960605407262080	2460518.7833	-111.44 ± 0.45	-109.91 ± 2.25		1.53 ± 2.29
2669312489313259008	2460561.6874	-126.95 ± 0.23	-65.99 ± 5.97	SNR	60.96 ± 5.97
2675008681099778944	2460510.7357	-202.49 ± 0.59	-197.30 ± 3.91		5.19 ± 3.95
2678479564430710656	2460623.5810	51.11 ± 0.27	46.95 ± 7.78		4.16 ± 7.78
2701466465622378496	2460481.8770	-419.66 ± 0.40	-421.43 ± 4.72		1.77 ± 4.74
2748452621862730240	2460629.6198	-268.00 ± 1.17	-262.00 ± 5.36		6.00 ± 5.49
2754870849189836800	2460560.7994	-87.81 ± 0.26	-92.04 ± 5.04		4.23 ± 5.05
2758595822787228928	2460627.5523	-201.22 ± 0.20	-200.71 ± 1.18		0.51 ± 1.20
2760474269683840256	2460560.7021	-191.48 ± 0.35	-192.62 ± 3.53		1.14 ± 3.54
2765690181047678336	2460519.7906	-28.81 ± 1.14	-25.81 ± 4.85		3.00 ± 4.98
2765690181047678336	2460568.7628	-19.30 ± 0.80	-25.81 ± 4.85		6.51 ± 4.91
2767395106968307712	2460624.6350	-161.32 ± 0.54	-160.05 ± 1.29		1.27 ± 1.40

**Table 3** *continued*

**Table 3** (*continued*)

<i>Gaia</i> DR3 ID	JD	RV	<i>Gaia</i> DR3 Mean RV	Flags	RV Shift
	d	km s <sup>-1</sup>	km s <sup>-1</sup>		km s <sup>-1</sup>
(1)	(2)	(3)	(4)	(5)	(6)
2781500952095012096	2460560.8361	-178.99 ± 0.35	-175.75 ± 2.65		3.24 ± 2.67
2781500952095012096	2460567.7614	-178.06 ± 0.38	-175.75 ± 2.65		2.31 ± 2.67
2782781024148048000	2460579.6568	42.16 ± 0.42	41.23 ± 2.40		0.93 ± 2.44
2783612048780246016	2460575.7886	-29.43 ± 2.15	-28.02 ± 4.77	SNR	1.41 ± 5.23
2788486767941706624	2460575.8055	-222.32 ± 0.66	-213.35 ± 5.21		8.97 ± 5.25
2788486767941706624	2460580.6963	-300.71 ± 0.58	-213.35 ± 5.21	SNR	87.36 ± 5.24
2788486767941706624	2460596.7702	-229.91 ± 0.53	-213.35 ± 5.21		16.56 ± 5.24
2788486767941706624	2460597.6688	-227.03 ± 0.39	-213.35 ± 5.21		13.68 ± 5.22
2801479903005558528	2460555.8271	-254.81 ± 0.06	-251.36 ± 1.23		3.45 ± 1.23
2801532198527486976	2460550.9327	-277.00 ± 0.18	-276.15 ± 1.77		0.85 ± 1.78
2828393130155180800	2460629.5372	-21.58 ± 1.23	-27.73 ± 13.45		6.15 ± 13.50
2835800093315146496	2460527.9174	-224.95 ± 0.23	-213.09 ± 3.03		11.86 ± 3.04
2835800093315146496	2460544.8193	-219.30 ± 0.15	-213.09 ± 3.03		6.21 ± 3.04
2843092157510956032	2460544.8543	-172.83 ± 0.21	-182.41 ± 3.62		9.58 ± 3.62
2843092157510956032	2460548.7996	-172.95 ± 0.21	-182.41 ± 3.62		9.46 ± 3.62
2865540508457717376	2460544.8737	-154.74 ± 0.11	-151.06 ± 2.28		3.68 ± 2.28
2892062618706914560	2460625.7524	235.99 ± 0.20	237.10 ± 2.42		1.11 ± 2.43
2896172215213785344	2460622.7905	144.49 ± 0.23	218.80 ± 4.09	SNR	74.31 ± 4.09
2896660398377207040	2460622.7726	280.54 ± 0.34	275.98 ± 2.89		4.56 ± 2.91
2899431683075290240	2460623.8294	147.37 ± 0.26	147.06 ± 5.41		0.31 ± 5.42
2905430824673932672	2460578.8818	86.54 ± 0.08	94.64 ± 1.46		8.10 ± 1.46
2912512023155224064	2460632.6903	70.05 ± 0.47	73.32 ± 3.16		3.27 ± 3.19
2949128990178535552	2460712.7325	-32.80 ± 0.38	61.40 ± 5.90	SNR	94.20 ± 5.91
2950822543021900288	2460712.7081	345.34 ± 0.60	347.53 ± 3.42		2.19 ± 3.48
2967475612996185728	2460632.6013	162.83 ± 0.50	122.54 ± 3.56	SNR	40.29 ± 3.60
2972713033554244480	2460623.7808	336.24 ± 0.25	340.62 ± 3.09		4.38 ± 3.10
3008540860462483456	2460632.6359	71.17 ± 0.66	70.92 ± 3.40	SNR	0.25 ± 3.46
3035481399307040384	2460428.5127	414.24 ± 0.06	416.28 ± 0.86		2.04 ± 0.86
3048420147209369600	2460732.6603	214.90 ± 0.95	220.09 ± 5.55		5.19 ± 5.63
3078328340945181952	2460428.4890	107.80 ± 0.18	104.17 ± 2.72		3.63 ± 2.72
3107577721076953216	2460735.6847	94.36 ± 1.10	113.59 ± 9.79	SNR	19.23 ± 9.86
3114270895026030720	2460734.5719	257.72 ± 1.07	323.57 ± 12.64	SNR	65.85 ± 12.68
3146951129379391232	2460735.6428	367.19 ± 0.16	368.66 ± 4.19	SNR	1.47 ± 4.20
3150574398150536832	2460734.6247	-14.65 ± 0.14	-64.36 ± 5.29	SNR	49.71 ± 5.29
3185179705568457344	2460626.7658	231.11 ± 0.77	215.60 ± 5.53	SB2	15.51 ± 5.59
3190523740098447744	2460572.8677	-46.45 ± 0.05	-65.92 ± 4.26		19.47 ± 4.26

**Table 3** *continued*

**Table 3** (*continued*)

<i>Gaia</i> DR3 ID	JD d	RV km s <sup>-1</sup>	<i>Gaia</i> DR3 Mean RV	Flags	RV Shift km s <sup>-1</sup>
			(4)		
(1)	(2)	(3)		(5)	(6)
3190523740098447744	2460574.8720	-55.24 ± 0.05	-65.92 ± 4.26		10.68 ± 4.26
3192689056450786304	2460572.8847	167.97 ± 0.11	160.92 ± 1.99	SB2	7.05 ± 1.99
3195269030422383488	2460622.7120	13.74 ± 0.93	29.14 ± 7.83		15.40 ± 7.88
3195269030422383488	2460633.5916	127.62 ± 0.66	29.14 ± 7.83	SNR	98.48 ± 7.85
3205847878470249088	2460624.6800	44.46 ± 0.18	41.85 ± 0.86		2.61 ± 0.88
3207170625318358784	2460424.4686	122.93 ± 0.35	122.48 ± 3.51		0.45 ± 3.53
3214683828787855360	2460624.6987	164.79 ± 1.73	160.32 ± 5.50		4.47 ± 5.76
3239331546588730752	2460630.6720	322.33 ± 0.87	322.78 ± 2.60		0.45 ± 2.75
3246885466349457536	2460572.8575	149.79 ± 0.05	142.20 ± 4.46		7.59 ± 4.46
3252546886080448384	2460622.7369	22.43 ± 0.14	4.52 ± 3.48		17.91 ± 3.48
3258029325934167168	2460629.7018	125.60 ± 1.01	125.21 ± 6.45		0.39 ± 6.53
3266994193990116608	2460572.8197	-101.25 ± 0.89	-95.25 ± 4.60		6.00 ± 4.68
3270069940330680576	2460559.8769	21.49 ± 0.54	10.78 ± 5.09		10.71 ± 5.12
3270069940330680576	2460580.8054	18.16 ± 0.49	10.78 ± 5.09		7.38 ± 5.11
3289282909594133120	2460630.6899	145.39 ± 0.26	152.84 ± 6.25		7.45 ± 6.26
3326250307290068224	2460712.6276	-100.05 ± 0.53	-97.86 ± 5.01		2.19 ± 5.04
3334451190860930816	2460632.7085	50.48 ± 0.63	51.56 ± 4.92		1.08 ± 4.96
3383997379534709504	2460579.9028	-32.46 ± 0.15	-31.86 ± 2.47		0.60 ± 2.48
3449708077060728832	2460579.0137	166.98 ± 0.06	164.67 ± 1.53		2.31 ± 1.53
3460512226209856128	2460449.6214	113.57 ± 1.08	113.93 ± 3.98		0.36 ± 4.13
3463596081447832704	2460740.6636	210.39 ± 0.59	250.80 ± 4.16	SNR	40.41 ± 4.20
3463596081447832704	2460740.6689	248.73 ± 0.66	250.80 ± 4.16	SNR	2.07 ± 4.21
3463780112206037120	2460449.5844	199.22 ± 0.86	190.16 ± 6.83		9.06 ± 6.89
3485639846475600000	2460733.7985	-1.40 ± 0.14	-2.26 ± 1.39		0.86 ± 1.40
3524477002349225984	2460740.6931	122.30 ± 0.26	69.25 ± 7.50	SNR	53.05 ± 7.51
3529854748080356352	2460509.4983	84.01 ± 0.05	99.61 ± 5.97		15.60 ± 5.97
3577444188310927744	2460427.6929	300.74 ± 0.15	296.96 ± 2.05		3.78 ± 2.06
3584915266743410048	2460459.5458	113.63 ± 0.87	114.29 ± 3.68		0.66 ± 3.78
3585663759283867008	2460479.5475	173.87 ± 0.93	172.28 ± 8.15		1.59 ± 8.20
3594336603925116672	2460739.7846	4.34 ± 1.07	5.04 ± 7.77	SNR	0.70 ± 7.84
3618015033504305408	2460733.8281	89.22 ± 0.39	91.21 ± 2.41		1.99 ± 2.44
3618107353825818880	2460425.7050	121.65 ± 0.08	120.57 ± 1.73		1.08 ± 1.73
3618107353825818880	2460509.5217	122.61 ± 0.12	120.57 ± 1.73		2.04 ± 1.73
3619929278952732928	2460481.6360	51.08 ± 0.69	39.05 ± 8.07		12.03 ± 8.10
3636369696502927104	2460739.8331	91.99 ± 0.18	97.31 ± 2.27		5.32 ± 2.27
3638399772924914176	2460480.5636	-88.54 ± 0.33	-77.50 ± 2.25		11.04 ± 2.27

**Table 3** *continued*

**Table 3** (*continued*)

<i>Gaia</i> DR3 ID	JD	RV	<i>Gaia</i> DR3 Mean RV	Flags	RV Shift
	d	km s <sup>-1</sup>	km s <sup>-1</sup>		km s <sup>-1</sup>
(1)	(2)	(3)	(4)	(5)	(6)
3651926239847699968	2460425.5988	$-122.44 \pm 0.08$	$-116.95 \pm 2.19$		$5.49 \pm 2.19$
3651926239847699968	2460509.5888	$-118.03 \pm 0.09$	$-116.95 \pm 2.19$		$1.08 \pm 2.19$
3655969212822303616	2460428.7253	$-105.01 \pm 0.30$	$-101.71 \pm 6.20$		$3.30 \pm 6.21$
3657930157450714752	2460428.6729	$-20.90 \pm 0.18$	$-13.16 \pm 4.24$		$7.74 \pm 4.25$
3679906268154294016	2460480.5422	$193.57 \pm 0.35$	$194.29 \pm 2.45$		$0.72 \pm 2.47$
3690660213428217344	2460462.5791	$72.29 \pm 0.47$	$75.50 \pm 3.30$		$3.21 \pm 3.33$
3718625668909565952	2460427.6692	$135.79 \pm 0.14$	$137.77 \pm 2.05$		$1.98 \pm 2.05$
3720871700582825088	2460485.6118	$16.27 \pm 0.78$	$7.81 \pm 8.75$		$8.46 \pm 8.79$
3736156767635254272	2460480.5043	$79.88 \pm 1.04$	$85.85 \pm 4.87$		$5.97 \pm 4.98$
3737235663419837568	2460462.5552	$-8.66 \pm 0.16$	$-9.26 \pm 1.95$		$0.60 \pm 1.96$
3737235663419837568	2460480.4853	$-8.57 \pm 0.27$	$-9.26 \pm 1.95$		$0.69 \pm 1.97$
3741881684162720768	2460481.4914	$-184.64 \pm 0.63$	$-190.76 \pm 4.29$		$6.12 \pm 4.34$
3816735508068512512	2460738.7418	$60.29 \pm 0.32$	$61.38 \pm 7.57$		$1.09 \pm 7.58$
3824738543969555840	2460449.4811	$194.31 \pm 0.35$	$192.87 \pm 37.83$		$1.44 \pm 37.84$
3832884821324406400	2460425.5153	$4.13 \pm 0.08$	$-9.43 \pm 2.40$	SB2	$13.56 \pm 2.40$
3832884821324406400	2460478.4713	$1.85 \pm 0.16$	$-9.43 \pm 2.40$	SB2	$11.28 \pm 2.40$
3838404232257203072	2460424.5229	$116.84 \pm 0.53$	$129.14 \pm 5.89$		$12.30 \pm 5.91$
3842494866483989120	2460449.4643	$45.86 \pm 0.42$	$44.81 \pm 3.42$		$1.05 \pm 3.45$
3850064076328182656	2460449.4980	$131.81 \pm 1.01$	$137.03 \pm 3.35$		$5.22 \pm 3.50$
3900567355515742976	2460425.5521	$59.83 \pm 0.09$	$47.56 \pm 2.79$	SB2	$12.27 \pm 2.79$
3900567355515742976	2460509.4580	$59.05 \pm 0.08$	$47.56 \pm 2.79$	SB2	$11.49 \pm 2.79$
3903598369771891072	2460459.5079	$159.99 \pm 0.50$	$166.65 \pm 2.39$		$6.66 \pm 2.44$
3906590175271460480	2460740.7203	$-78.54 \pm 1.01$	$-71.49 \pm 8.15$	SNR	$7.05 \pm 8.21$
3931304688402594176	2460481.4648	$58.64 \pm 0.65$	$49.07 \pm 8.04$		$9.57 \pm 8.06$
4036323751356613120	2460517.6421	$-302.90 \pm 0.60$	$-313.37 \pm 6.79$		$10.47 \pm 6.82$
4036323751356613120	2460599.4986	$-300.32 \pm 0.45$	$-313.37 \pm 6.79$		$13.05 \pm 6.81$
4037752218725563392	2460738.8551	$168.70 \pm 0.20$	$173.47 \pm 6.44$		$4.77 \pm 6.44$
4078664878917893632	2460427.8245	$26.52 \pm 0.53$	$-57.81 \pm 11.28$	$v \sin i$	$84.33 \pm 11.30$
4219851655185139328	2460560.6612	$-340.98 \pm 0.63$	$-338.97 \pm 3.99$		$2.01 \pm 4.04$
4229000828879015936	2460509.7532	$-50.01 \pm 0.18$	$-44.46 \pm 5.60$		$5.55 \pm 5.61$
4242596049637833472	2460509.7196	$-290.96 \pm 0.25$	$-300.47 \pm 4.99$		$9.51 \pm 4.99$
4242596049637833472	2460624.5232	$-298.97 \pm 1.15$	$-300.47 \pm 4.99$		$1.50 \pm 5.12$
4243579356635038336	2460428.8829	$-334.36 \pm 0.13$	$-334.24 \pm 1.23$		$0.12 \pm 1.24$
4297175497614395008	2460518.7477	$6.02 \pm 0.91$	$-25.57 \pm 6.00$	SNR	$31.59 \pm 6.07$
4297175497614395008	2460599.5244	$-22.06 \pm 1.04$	$-25.57 \pm 6.00$		$3.51 \pm 6.09$
4311422866241470080	2460515.6762	$2.77 \pm 0.63$	$-1.94 \pm 4.90$		$4.71 \pm 4.94$

**Table 3** *continued*

**Table 3** (*continued*)

<i>Gaia</i> DR3 ID	JD d	RV km s <sup>-1</sup>	<i>Gaia</i> DR3 Mean RV km s <sup>-1</sup>	Flags	RV Shift km s <sup>-1</sup>
(1)	(2)	(3)	(4)	(5)	(6)
4318465066420528000	2460425.8072	$-358.38 \pm 0.03$	$-333.18 \pm 3.38$		$25.20 \pm 3.38$
4318465066420528000	2460459.8523	$-357.66 \pm 0.09$	$-333.18 \pm 3.38$		$24.48 \pm 3.38$
4324114150961924992	2460462.7388	$49.69 \pm 0.38$	$36.46 \pm 1.03$		$13.23 \pm 1.10$
4324114150961924992	2460736.8534	$41.92 \pm 0.15$	$36.46 \pm 1.03$		$5.46 \pm 1.04$
4341979565646134016	2460478.7052	$35.15 \pm 0.32$	$37.61 \pm 4.52$		$2.46 \pm 4.53$
4344582418904624256	2460479.6968	$237.59 \pm 0.33$	$226.13 \pm 9.81$		$11.46 \pm 9.82$
4399319028313941760	2460485.6876	$-60.33 \pm 0.84$	$-53.10 \pm 3.42$		$7.23 \pm 3.52$
4404085239419591552	2460428.7591	$-187.95 \pm 0.39$	$-200.46 \pm 2.46$		$12.51 \pm 2.49$
4404085239419591552	2460736.8124	$-209.34 \pm 1.34$	$-200.46 \pm 2.46$		$8.88 \pm 2.81$
4406004814924526848	2460425.7244	$-39.68 \pm 0.11$	$-42.11 \pm 2.08$		$2.43 \pm 2.09$
4406004814924526848	2460569.4858	$-42.56 \pm 0.11$	$-42.11 \pm 2.08$		$0.45 \pm 2.09$
4419230084377663744	2460736.8702	$-90.96 \pm 0.57$	$-94.50 \pm 5.09$		$3.54 \pm 5.12$
4449971364341398272	2460424.7693	$-166.72 \pm 0.42$	$-149.89 \pm 6.44$		$16.83 \pm 6.45$
4449971364341398272	2460459.7247	$-164.68 \pm 0.47$	$-149.89 \pm 6.44$		$14.79 \pm 6.45$
4449971364341398272	2460739.8754	$-161.65 \pm 0.56$	$-149.89 \pm 6.44$		$11.76 \pm 6.46$
4458199593966253184	2460462.7074	$-183.49 \pm 0.17$	$-193.15 \pm 30.51$		$9.66 \pm 30.51$
4458378470765084928	2460428.7764	$-84.98 \pm 0.14$	$-83.24 \pm 2.19$		$1.74 \pm 2.19$
4458669910066960384	2460424.7862	$-48.51 \pm 1.31$	$-79.56 \pm 6.33$	SB2	$31.05 \pm 6.46$
4458669910066960384	2460481.7005	$-58.89 \pm 0.89$	$-79.56 \pm 6.33$	SB2	$20.67 \pm 6.39$
4462674224036731392	2460428.7930	$22.95 \pm 0.30$	$30.24 \pm 1.96$		$7.29 \pm 1.98$
4463022464283196928	2460485.6700	$-206.62 \pm 0.69$	$-195.49 \pm 4.30$		$11.13 \pm 4.35$
4464923863483932672	2460478.6252	$-147.43 \pm 0.51$	$-140.83 \pm 1.97$		$6.60 \pm 2.04$
4465345320035111424	2460485.6531	$-161.72 \pm 0.42$	$-162.71 \pm 4.22$		$0.99 \pm 4.24$
4466423837863123328	2460478.6553	$-313.02 \pm 0.63$	$-336.00 \pm 4.36$		$22.98 \pm 4.41$
4466423837863123328	2460521.5944	$-315.93 \pm 1.05$	$-336.00 \pm 4.36$		$20.07 \pm 4.49$
4466423837863123328	2460560.5017	$-318.12 \pm 1.11$	$-336.00 \pm 4.36$		$17.88 \pm 4.50$
4466423837863123328	2460740.8790	$-367.20 \pm 0.01$	$-336.00 \pm 4.36$	SNR	$31.20 \pm 4.36$
4480417902167849728	2460425.7865	$-196.98 \pm 0.08$	$-208.32 \pm 2.86$		$11.34 \pm 2.87$
4480417902167849728	2460513.5853	$-198.42 \pm 0.11$	$-208.32 \pm 2.86$		$9.90 \pm 2.87$
4480417902167849728	2460600.4939	$-216.63 \pm 0.14$	$-208.32 \pm 2.86$		$8.31 \pm 2.87$
4486716699344464640	2460464.7472	$123.60 \pm 0.32$	$116.76 \pm 5.46$		$6.84 \pm 5.47$
4526671921107968640	2460509.6333	$-10.52 \pm 0.95$	$-20.99 \pm 6.90$	SB2	$10.47 \pm 6.96$
4556877979423587456	2460536.7213	$-506.33 \pm 0.28$	$-499.91 \pm 5.77$		$6.42 \pm 5.78$
4568304825812360064	2460573.7711	$-223.65 \pm 0.11$	$-222.13 \pm 0.95$		$1.52 \pm 0.96$
4575229962359762176	2460575.7399	$-29.23 \pm 0.24$	$-27.23 \pm 1.63$		$2.00 \pm 1.65$
4596554062668403328	2460568.7210	$-123.99 \pm 0.36$	$-115.86 \pm 5.60$		$8.13 \pm 5.61$

**Table 3** *continued*

**Table 3** (*continued*)

<i>Gaia</i> DR3 ID	JD d	RV km s <sup>-1</sup>	<i>Gaia</i> DR3 Mean RV	Flags	RV Shift km s <sup>-1</sup>
			(4)		
(1)	(2)	(3)		(5)	(6)
4600988839738641664	2460574.7754	$-21.44 \pm 0.24$	$-22.94 \pm 4.22$		$1.50 \pm 4.23$
4605537828581921792	2460560.7393	$-326.47 \pm 0.13$	$-328.30 \pm 3.21$		$1.83 \pm 3.21$
4615537233999076608	2460623.7010	$293.91 \pm 0.64$	$286.25 \pm 3.41$		$7.66 \pm 3.47$
4618585973584829440	2460575.8436	$176.39 \pm 0.89$	$185.15 \pm 4.21$		$8.76 \pm 4.30$
4623987839851960576	2460632.5755	$52.93 \pm 0.62$	$49.00 \pm 5.89$		$3.93 \pm 5.92$
4625065361248005248	2460630.7150	$28.52 \pm 1.04$	$30.29 \pm 8.42$		$1.77 \pm 8.48$
4630416817482099712	2460623.7181	$133.21 \pm 0.51$	$134.79 \pm 2.49$		$1.58 \pm 2.54$
4633036202073128448	2460571.8692	$172.68 \pm 0.23$	$158.88 \pm 5.60$	SB2	$13.80 \pm 5.61$
4651827199427540224	2460632.5580	$248.60 \pm 0.47$	$245.12 \pm 4.64$		$3.48 \pm 4.66$
4661235445562538112	2460625.6956	$27.81 \pm 0.44$	$34.23 \pm 3.50$		$6.42 \pm 3.52$
4674062382519374208	2460629.7191	$-10.06 \pm 1.19$	$54.51 \pm 4.72$	SNR	$64.57 \pm 4.87$
4678849484347880576	2460576.8317	$289.88 \pm 0.70$	$286.28 \pm 7.19$		$3.60 \pm 7.23$
4695299002933110272	2460627.6790	$130.04 \pm 0.77$	$133.15 \pm 6.98$		$3.11 \pm 7.02$
4696753927398383872	2460624.6560	$98.79 \pm 0.80$	$96.85 \pm 8.70$		$1.94 \pm 8.73$
4696981290083296640	2460569.8351	$37.69 \pm 0.23$	$41.11 \pm 3.05$		$3.42 \pm 3.06$
4705880840277690624	2460627.7031	$34.73 \pm 0.17$	$36.82 \pm 1.86$		$2.09 \pm 1.86$
4710671206281480192	2460569.7286	$153.75 \pm 0.26$	$156.27 \pm 3.89$		$2.52 \pm 3.90$
4719110473421285888	2460561.7768	$190.27 \pm 0.21$	$190.27 \pm 2.24$		$0.00 \pm 2.25$
4719110473421285888	2460574.8098	$191.02 \pm 0.20$	$190.27 \pm 2.24$		$0.75 \pm 2.25$
4721517579251891712	2460570.8754	$120.74 \pm 0.89$	$118.64 \pm 5.86$		$2.10 \pm 5.92$
4728502295587116160	2460626.6800	$89.25 \pm 0.62$	$90.02 \pm 5.37$		$0.77 \pm 5.41$
4738910650613013120	2460569.7929	$121.46 \pm 0.12$	$123.20 \pm 1.54$		$1.74 \pm 1.54$
4739893854526425216	2460570.7776	$-31.90 \pm 0.65$	$-29.56 \pm 7.03$		$2.34 \pm 7.06$
4746302632927184128	2460559.8940	$73.45 \pm 0.08$	$77.20 \pm 1.43$		$3.75 \pm 1.43$
4746302632927184128	2460569.7828	$72.79 \pm 0.03$	$77.20 \pm 1.43$		$4.41 \pm 1.43$
4751527580901330816	2460579.7541	$246.77 \pm 0.72$	$242.33 \pm 5.83$		$4.44 \pm 5.87$
4753774261113868416	2460571.8471	$144.59 \pm 0.42$	$139.01 \pm 3.96$		$5.58 \pm 3.98$
4757764182654737792	2460625.7319	$173.21 \pm 0.08$	$172.28 \pm 1.88$		$0.93 \pm 1.88$
4762898249119670400	2460631.5962	$132.90 \pm 0.38$	$129.05 \pm 4.46$		$3.85 \pm 4.47$
4770375340505228928	2460632.6728	$153.79 \pm 0.26$	$156.22 \pm 1.40$		$2.43 \pm 1.42$
4775145228104639232	2460578.8424	$328.31 \pm 0.09$	$333.41 \pm 1.13$		$5.10 \pm 1.13$
4777669947320442752	2460626.8083	$78.05 \pm 0.41$	$78.89 \pm 8.19$		$0.84 \pm 8.20$
4790283098038091008	2460630.6147	$187.87 \pm 0.23$	$190.03 \pm 4.62$		$2.16 \pm 4.63$
4791430335342393600	2460626.7068	$37.79 \pm 0.21$	$39.55 \pm 3.34$		$1.76 \pm 3.35$
4792163228561925504	2460631.6130	$20.64 \pm 0.67$	$8.67 \pm 5.15$		$11.97 \pm 5.20$
4798980303733591552	2460632.6550	$327.06 \pm 0.61$	$330.48 \pm 3.99$		$3.42 \pm 4.04$

**Table 3** *continued*

**Table 3** (*continued*)

<i>Gaia</i> DR3 ID	JD d	RV km s <sup>-1</sup>	<i>Gaia</i> DR3 Mean RV	Flags	RV Shift km s <sup>-1</sup>
			(4)		
(1)	(2)	(3)	(4)	(5)	(6)
4801894284424445056	2460623.7628	462.25 ± 0.54	463.24 ± 2.43		0.99 ± 2.49
4803825026843762560	2460632.6187	164.62 ± 0.53	155.84 ± 3.34		8.78 ± 3.39
4805795901436022784	2460622.8149	294.60 ± 0.49	296.55 ± 2.96		1.95 ± 3.00
4810532769327201792	2460630.6463	104.59 ± 0.41	102.99 ± 6.53		1.60 ± 6.54
4814070963385616384	2460600.8083	78.66 ± 0.38	82.89 ± 2.85		4.23 ± 2.88
4815626737978833792	2460630.5977	91.35 ± 0.44	91.17 ± 3.61		0.18 ± 3.64
4835367335384068352	2460598.7637	76.02 ± 0.56	67.26 ± 7.71		8.76 ± 7.73
4841632386998925440	2460630.5618	123.00 ± 0.30	122.22 ± 1.79		0.78 ± 1.82
4867178886835317376	2460573.8848	300.16 ± 0.24	293.86 ± 4.08		6.30 ± 4.09
4880417797108293632	2460578.8239	263.64 ± 0.10	261.27 ± 2.36		2.37 ± 2.36
4880744901817831552	2460578.8602	262.87 ± 0.27	266.86 ± 3.15		3.99 ± 3.17
4884385694054284672	2460630.5446	93.04 ± 0.45	97.63 ± 1.98		4.59 ± 2.03
4885231081056967168	2460622.6869	110.42 ± 0.36	108.52 ± 4.77		1.90 ± 4.78
4902931740794761728	2460599.7656	18.61 ± 0.07	18.07 ± 1.80		0.54 ± 1.80
4903248017890484608	2460568.6480	149.34 ± 0.23	149.67 ± 0.89		0.33 ± 0.92
4906613008803987456	2460560.8557	134.79 ± 0.72	132.81 ± 3.39		1.98 ± 3.46
4912541472422371840	2460561.8290	138.14 ± 2.21	128.27 ± 5.64	SNR	9.87 ± 6.06
4929840157581555840	2460598.6608	76.69 ± 0.24	70.04 ± 5.82		6.65 ± 5.82
4938691501062803072	2460570.7608	186.51 ± 2.27	187.23 ± 5.82		0.72 ± 6.25
4950010114277787776	2460567.6458	191.94 ± 0.14	192.48 ± 1.97		0.54 ± 1.98
4951630313380205952	2460621.6450	84.22 ± 0.36	80.22 ± 4.22		4.00 ± 4.23
4965484503487580032	2460571.8857	121.64 ± 0.42	121.76 ± 3.15		0.12 ± 3.17
4967858555250886272	2460568.8840	88.71 ± 0.12	83.79 ± 1.29		4.92 ± 1.30
4973715889913402112	2460598.6233	45.01 ± 0.09	45.13 ± 0.67		0.12 ± 0.67
4978614355950125696	2460517.9003	-35.61 ± 0.45	8.07 ± 4.35	SB2	43.68 ± 4.37
4978614355950125696	2460518.9095	-40.05 ± 1.04	8.07 ± 4.35	SB2	48.12 ± 4.47
4978614355950125696	2460520.8754	34.95 ± 0.39	8.07 ± 4.35	SB2	26.88 ± 4.37
4992290493893169664	2460560.8173	120.11 ± 0.41	112.40 ± 3.40		7.71 ± 3.43
5000838062927554176	2460598.6416	103.09 ± 0.24	91.90 ± 2.39		11.19 ± 2.40
5034075646601072000	2460567.8279	-102.29 ± 0.15	-76.64 ± 2.25	SB2	25.65 ± 2.25
5035314860629134080	2460567.8440	-68.50 ± 0.12	-67.00 ± 3.76		1.50 ± 3.76
5035671519008704256	2460600.7171	-6.40 ± 0.30	-0.74 ± 10.96		5.66 ± 10.97
5039157932941255296	2460626.6611	-13.85 ± 0.15	-8.88 ± 1.95		4.97 ± 1.95
5041854072891578496	2460580.7792	38.52 ± 0.66	51.63 ± 7.98	SNR	13.11 ± 8.01
5042687811943245184	2460578.7452	90.24 ± 0.27	94.80 ± 6.73		4.56 ± 6.74
5044327218140737536	2460629.7470	182.51 ± 0.65	205.68 ± 13.26		23.17 ± 13.27

**Table 3** *continued*

**Table 3** (*continued*)

<i>Gaia</i> DR3 ID	JD d	RV km s <sup>-1</sup>	<i>Gaia</i> DR3 Mean RV	Flags	RV Shift km s <sup>-1</sup>
			(4)		
(1)	(2)	(3)		(5)	(6)
5044327218140737536	2460633.5674	181.28 ± 0.86	205.68 ± 13.26	SNR	24.40 ± 13.29
5059047789053289856	2460571.8031	26.60 ± 0.30	15.65 ± 1.78		10.95 ± 1.81
5082958696621785984	2460600.7910	59.14 ± 0.11	63.16 ± 1.14		4.02 ± 1.15
5083871359992456448	2460572.8370	162.17 ± 0.11	161.99 ± 1.76		0.18 ± 1.76
5089796971751769856	2460600.7431	72.59 ± 0.06	74.86 ± 1.59		2.27 ± 1.59
5094819506507559296	2460578.7690	-78.09 ± 0.27	-75.21 ± 5.93		2.88 ± 5.94
5119215607942562944	2460621.6725	214.06 ± 0.15	216.09 ± 2.47		2.03 ± 2.48
5139848390314545792	2460628.7160	116.46 ± 0.17	69.86 ± 1.91	SNR	46.60 ± 1.91
5139848390314545792	2460629.6845	69.36 ± 0.24	69.86 ± 1.91		0.50 ± 1.92
5141607437120133248	2460561.8114	89.97 ± 0.29	89.40 ± 4.44		0.57 ± 4.45
5157067189081730560	2460570.8016	32.10 ± 1.29	32.67 ± 5.02		0.57 ± 5.18
5158765384790885760	2460571.8241	-14.45 ± 0.26	-14.57 ± 3.00		0.12 ± 3.01
5183256525263276288	2460599.8495	-69.45 ± 0.32	-67.76 ± 3.19		1.69 ± 3.21
5186664770791126912	2460572.8019	133.24 ± 0.36	122.56 ± 2.81		10.68 ± 2.84
5188617434724794624	2460450.5197	170.13 ± 1.17	168.60 ± 7.24	SNR	1.53 ± 7.34
5195206189434712064	2460738.6450	19.40 ± 0.17	4.14 ± 17.13	SNR	15.26 ± 17.13
5196065870088374656	2460738.6683	88.82 ± 0.68	90.51 ± 17.42	SNR	1.69 ± 17.43
5197671122705982080	2460448.5942	334.68 ± 0.40	332.97 ± 2.42		1.71 ± 2.46
5202922905635808640	2460448.5353	147.14 ± 0.42	149.42 ± 2.37		2.28 ± 2.40
5240547605125005696	2460428.6183	0.39 ± 0.31	9.57 ± 21.50	hot	9.18 ± 21.50
5274125526303605376	2460735.7869	68.58 ± 0.11	65.19 ± 9.83	SNR	3.39 ± 9.83
5300091008802250112	2460449.5324	261.66 ± 1.48	251.25 ± 4.40		10.41 ± 4.64
5321281033104697088	2460450.5021	227.50 ± 0.33	231.79 ± 2.04		4.29 ± 2.06
5326941941734897024	2460425.4877	27.64 ± 0.02	16.84 ± 5.16	hot	10.80 ± 5.16
5327915383187030784	2460459.4617	168.27 ± 0.90	168.84 ± 7.15	SNR	0.57 ± 7.20
5334791939429604608	2460479.5963	170.74 ± 0.54	175.72 ± 6.24	SNR	4.98 ± 6.26
5335252737865276032	2460427.5913	267.39 ± 0.24	269.73 ± 7.55		2.34 ± 7.56
5336819782417836288	2460425.5348	-1.36 ± 0.09	-2.89 ± 3.00	hot	1.53 ± 3.00
5336819782417836288	2460509.4754	-16.06 ± 0.12	-2.89 ± 3.00	hot	13.17 ± 3.00
5348155781656154880	2460739.7578	73.09 ± 0.35	65.23 ± 13.56		7.86 ± 13.56
5356371259506596480	2460428.5749	-91.54 ± 0.33	-12.46 ± 7.05	hot	79.08 ± 7.06
5356567870254195328	2460425.4979	24.18 ± 0.35	2.76 ± 20.12	hot	21.42 ± 20.12
5356567870254195328	2460478.4882	-81.39 ± 1.29	2.76 ± 20.12	hot	84.15 ± 20.16
5359619839640581376	2460479.5292	45.75 ± 0.48	-29.52 ± 16.60	hot	75.27 ± 16.61
5367299790914345984	2460448.5697	92.37 ± 0.84	97.53 ± 4.03	SNR	5.16 ± 4.11
5371704297057727232	2460449.6010	322.59 ± 0.37	324.93 ± 2.41		2.34 ± 2.44

**Table 3** *continued*

**Table 3** (*continued*)

<i>Gaia</i> DR3 ID	JD d	RV km s <sup>-1</sup>	<i>Gaia</i> DR3 Mean RV	Flags	RV Shift km s <sup>-1</sup>
			(4)		
(1)	(2)	(3)		(5)	(6)
5376423126081823360	2460448.6549	267.28 ± 1.66	358.87 ± 4.39	SNR	91.59 ± 4.70
5376693704723955840	2460450.5929	207.03 ± 0.51	191.19 ± 7.53	SNR	15.84 ± 7.55
5393856089096403840	2460427.6155	123.02 ± 0.23	131.72 ± 4.29		8.70 ± 4.29
5393856089096403840	2460448.6306	121.88 ± 0.35	131.72 ± 4.29		9.84 ± 4.30
5399604438965438848	2460740.6289	128.53 ± 0.68	213.70 ± 5.99	SNR	85.17 ± 6.03
5399748818585456768	2460741.8163	297.58 ± 1.99	254.76 ± 6.39	SNR	42.82 ± 6.69
5400128459336707072	2460449.5675	77.61 ± 0.29	80.22 ± 2.75		2.61 ± 2.77
5432677164616070144	2460739.7213	313.90 ± 0.46	315.67 ± 3.46		1.77 ± 3.49
5437197703594043648	2460448.5527	55.86 ± 0.63	51.48 ± 2.99		4.38 ± 3.05
5470326985368066304	2460448.6137	104.71 ± 0.72	87.58 ± 7.48		17.13 ± 7.51
5485223065822432000	2460731.6028	220.58 ± 0.39	216.80 ± 4.47		3.78 ± 4.49
5491120949273989248	2460732.6335	116.98 ± 0.27	114.43 ± 6.79		2.55 ± 6.80
5509286152674973184	2460731.6429	112.19 ± 0.35	110.89 ± 3.50		1.30 ± 3.51
5510992972680488832	2460735.7635	150.43 ± 0.65	136.99 ± 6.07		13.44 ± 6.11
5533294878122904448	2460450.4765	330.06 ± 0.40	324.36 ± 3.82		5.70 ± 3.84
5558621205053610368	2460625.7764	294.63 ± 0.15	292.62 ± 2.18		2.01 ± 2.19
5560933512367258752	2460625.7935	161.00 ± 0.33	158.36 ± 4.91		2.64 ± 4.92
5575760254868795136	2460633.8033	176.91 ± 0.83	175.29 ± 3.48		1.62 ± 3.58
5580281034364803072	2460633.7614	174.90 ± 0.42	172.26 ± 3.70		2.64 ± 3.72
5604520833353953280	2460735.6605	170.25 ± 0.90	167.22 ± 4.33	SNR	3.03 ± 4.42
5614140632394855680	2460735.7389	191.32 ± 0.45	189.70 ± 3.89		1.62 ± 3.91
5688075127125733504	2460449.5152	301.19 ± 0.73	306.59 ± 4.31		5.40 ± 4.37
5713661999660822016	2460738.5335	179.77 ± 0.69	176.80 ± 8.44		2.97 ± 8.47
5735304576081570048	2460738.7175	-13.21 ± 0.69	-7.63 ± 6.54		5.58 ± 6.57
5761883109315557888	2460739.6874	66.84 ± 0.81	64.53 ± 4.97		2.31 ± 5.03
5764114052767463680	2460740.5763	-33.29 ± 1.49	-36.56 ± 5.94	SNR	3.27 ± 6.13
5767212132939510400	2460425.7434	119.42 ± 0.15	126.17 ± 1.38		6.75 ± 1.39
5767212132939510400	2460481.7543	108.62 ± 0.23	126.17 ± 1.38		17.55 ± 1.40
5767212132939510400	2460736.8360	128.60 ± 0.17	126.17 ± 1.38		2.43 ± 1.39
5770704628546574848	2460481.5334	108.23 ± 1.73	105.74 ± 5.07	SNR	2.49 ± 5.35
5772808715845778176	2460519.5012	343.37 ± 0.04	293.87 ± 6.60	SNR	49.50 ± 6.60
5783922338860010368	2460479.5723	88.46 ± 0.63	92.90 ± 4.01		4.44 ± 4.06
5817399066319766912	2460485.7703	-51.73 ± 0.92	-32.23 ± 5.38		19.50 ± 5.46
5817399066319766912	2460598.5128	-48.64 ± 0.53	-32.23 ± 5.38		16.41 ± 5.41
5831887605960848000	2460738.8314	77.94 ± 0.80	68.98 ± 6.40		8.96 ± 6.45
5832426023053419648	2460478.6800	128.47 ± 0.42	136.06 ± 6.55		7.59 ± 6.57

**Table 3** *continued*

**Table 3** (*continued*)

<i>Gaia</i> DR3 ID	JD d	RV km s <sup>-1</sup>	<i>Gaia</i> DR3 Mean RV	Flags	RV Shift km s <sup>-1</sup>
			(4)		
(1)	(2)	(3)	(4)	(5)	(6)
5842093547727016960	2460510.4699	19.20 ± 0.80	-22.32 ± 10.73	SNR	41.52 ± 10.76
5851089266522263936	2460509.5721	219.05 ± 0.27	223.70 ± 2.64		4.65 ± 2.66
5858256226910097536	2460448.6798	11.43 ± 0.82	14.70 ± 3.57		3.27 ± 3.66
5889520363370193536	2460738.8074	-94.12 ± 0.44	-80.83 ± 7.11		13.29 ± 7.13
5915536178508998784	2460425.7672	-17.91 ± 0.06	-21.42 ± 1.06		3.51 ± 1.06
5915536178508998784	2460510.6934	-22.59 ± 0.09	-21.42 ± 1.06		1.17 ± 1.06
5916840787735273216	2460464.7714	265.42 ± 0.72	262.12 ± 4.18		3.30 ± 4.24
5923359031943461120	2460462.8226	111.82 ± 0.21	114.94 ± 3.49		3.12 ± 3.49
5923503450243018752	2460428.8116	152.36 ± 0.42	147.23 ± 2.89		5.13 ± 2.93
6039722860077339136	2460740.8552	-56.81 ± 0.47	-58.98 ± 4.69		2.17 ± 4.71
6072111685190490112	2460480.5216	-7.06 ± 0.45	-5.65 ± 38.54	hot	1.41 ± 38.54
6082341236436152576	2460740.7465	0.61 ± 0.36	7.29 ± 2.71		6.68 ± 2.73
6104480246655766016	2460741.8774	-76.56 ± 1.29	-5.38 ± 6.37	SNR	71.18 ± 6.50
6104628783805040384	2460518.5807	-1.73 ± 2.10	-24.38 ± 8.50	SNR	22.65 ± 8.76
6104628783805040384	2460712.7988	-3.44 ± 0.72	-24.38 ± 8.50	SNR	20.94 ± 8.53
6109390489486849408	2460427.7891	101.20 ± 0.11	99.43 ± 2.59		1.77 ± 2.59
6117757983437538432	2460510.6131	157.49 ± 0.83	153.44 ± 5.57		4.05 ± 5.63
6118173976785581568	2460740.8137	1.89 ± 0.39	-2.08 ± 4.95		3.97 ± 4.97
6133984369878480128	2460739.8093	116.96 ± 0.33	116.28 ± 4.01		0.68 ± 4.03
6134138267147056768	2460733.7462	-16.13 ± 0.44	-20.66 ± 3.14		4.53 ± 3.17
6140717877864676352	2460481.6117	45.69 ± 0.44	49.92 ± 7.78		4.23 ± 7.80
6154038774769241600	2460428.6558	370.82 ± 0.36	369.77 ± 2.69		1.05 ± 2.71
6157786696375384064	2460428.6359	279.97 ± 0.13	285.28 ± 3.97		5.31 ± 3.98
6165452942416452864	2460449.6425	81.43 ± 0.48	73.36 ± 2.22		8.07 ± 2.27
6177352097769902208	2460428.7071	-46.58 ± 0.26	-62.66 ± 4.00		16.08 ± 4.01
6177352097769902208	2460712.7814	-64.88 ± 0.53	-62.66 ± 4.00		2.22 ± 4.03
6188708953373074048	2460449.6612	-11.35 ± 0.26	-7.69 ± 3.90		3.66 ± 3.91
6214736008513502976	2460510.6375	-59.62 ± 0.56	-62.89 ± 7.75		3.27 ± 7.77
6235652499248057728	2460462.7896	-34.42 ± 0.29	-41.77 ± 2.72		7.35 ± 2.73
6275466158880793856	2460427.7231	29.82 ± 0.18	24.51 ± 2.42	v sin i	5.31 ± 2.43
6275708429396071936	2460510.5707	159.32 ± 0.27	157.19 ± 3.66		2.13 ± 3.67
6288565568615343488	2460739.8496	-28.83 ± 0.48	-17.72 ± 7.79		11.11 ± 7.81
6289559179234696960	2460428.6904	-2.89 ± 0.12	-6.01 ± 3.13		3.12 ± 3.13
6319928416243214464	2460515.6266	12.59 ± 1.74	7.58 ± 17.18	SNR	5.01 ± 17.27
6349293863560840576	2460519.6773	-13.75 ± 2.46	-11.77 ± 6.44	SNR	1.98 ± 6.90
6368640114249326976	2460481.8249	5.09 ± 0.27	4.49 ± 2.31		0.60 ± 2.33

**Table 3** *continued*

**Table 3** (*continued*)

<i>Gaia</i> DR3 ID	JD	RV	<i>Gaia</i> DR3 Mean RV	Flags	RV Shift
	d	km s <sup>-1</sup>	km s <sup>-1</sup>		km s <sup>-1</sup>
(1)	(2)	(3)	(4)	(5)	(6)
6374547824585473536	2460480.7590	-34.06 ± 0.50	-38.05 ± 2.50		3.99 ± 2.55
6375836074255319936	2460479.8875	-53.92 ± 0.65	-60.10 ± 1.64		6.18 ± 1.77
6393888749512565760	2460513.8346	104.85 ± 0.09	65.91 ± 3.57		38.94 ± 3.57
6393888749512565760	2460623.6078	73.38 ± 0.68	65.91 ± 3.57		7.47 ± 3.64
6402359833770432512	2460510.7112	168.87 ± 1.17	166.14 ± 5.06		2.73 ± 5.20
6402817333686791296	2460485.8242	37.28 ± 0.62	28.04 ± 3.08		9.24 ± 3.14
6402817333686791296	2460623.5634	42.80 ± 0.33	28.04 ± 3.08		14.76 ± 3.09
6402817333686791296	2460633.5385	43.13 ± 0.72	28.04 ± 3.08		15.09 ± 3.16
6403003597828842240	2460481.8594	-31.04 ± 0.15	-35.42 ± 2.33		4.38 ± 2.34
6409038026880037376	2460622.6178	46.96 ± 0.57	54.25 ± 5.17		7.29 ± 5.20
6420147904684678144	2460479.7509	67.70 ± 0.60	66.98 ± 6.16		0.72 ± 6.19
6420303519939663488	2460625.5259	-4.32 ± 0.39	-5.10 ± 7.75		0.78 ± 7.76
6421461168246828032	2460599.6064	227.29 ± 0.38	228.37 ± 3.40		1.08 ± 3.42
6421465531933455360	2460428.9004	-102.00 ± 0.08	-105.72 ± 0.99		3.72 ± 0.99
6422752304132663680	2460479.7769	-7.15 ± 0.66	-16.03 ± 8.64		8.88 ± 8.66
6431108077108143488	2460599.6533	-154.94 ± 0.38	-155.28 ± 3.69		0.34 ± 3.71
6433084105663790080	2460464.7950	166.86 ± 0.50	171.21 ± 3.45		4.35 ± 3.49
6445023942945668992	2460427.8556	167.68 ± 0.12	167.17 ± 1.94		0.51 ± 1.94
6451215048105801216	2460461.9004	-92.91 ± 0.06	-91.95 ± 1.78		0.96 ± 1.79
6457366957398956928	2460481.8071	183.91 ± 0.53	185.56 ± 2.66		1.65 ± 2.71
6463410835377385472	2460558.5699	22.19 ± 0.55	0.77 ± 5.02		21.42 ± 5.05
6463410835377385472	2460575.5925	16.76 ± 0.63	0.77 ± 5.02		15.99 ± 5.06
6463410835377385472	2460622.5698	7.34 ± 0.70	0.77 ± 5.02	SNR	6.57 ± 5.07
6469982100983952896	2460623.5466	299.32 ± 0.12	298.89 ± 2.25		0.43 ± 2.25
6473015344324423680	2460464.8681	-210.71 ± 0.20	-210.65 ± 6.03		0.06 ± 6.04
6477293200470828288	2460481.8421	215.99 ± 0.32	213.98 ± 2.96		2.01 ± 2.98
6484717029965817984	2460462.9089	-30.49 ± 0.11	-33.19 ± 2.20		2.70 ± 2.20
6484717029965817984	2460478.8932	-31.00 ± 0.35	-33.19 ± 2.20		2.19 ± 2.23
6487033842699994496	2460599.7248	17.28 ± 0.43	10.79 ± 3.67		6.49 ± 3.70
6492216047160201728	2460623.6514	174.14 ± 0.54	183.55 ± 4.82		9.41 ± 4.85
6504574764016144896	2460513.8178	145.87 ± 0.39	141.49 ± 2.33		4.38 ± 2.36
6508841693764232704	2460510.7589	188.62 ± 0.47	193.12 ± 3.84		4.50 ± 3.87
6520467998436840448	2460510.7930	30.81 ± 0.50	25.47 ± 5.99		5.34 ± 6.01
6528915614992166528	2460513.8638	5.24 ± 0.92	3.95 ± 5.96	SNR	1.29 ± 6.03
6532929794505116800	2460622.6419	-43.38 ± 0.44	-41.01 ± 4.72		2.37 ± 4.74
6534773125749528960	2460626.6443	36.54 ± 0.17	36.89 ± 3.87		0.35 ± 3.87

**Table 3** *continued*

**Table 3** (*continued*)

<i>Gaia</i> DR3 ID	JD	RV	<i>Gaia</i> DR3 Mean RV	Flags	RV Shift
	d	km s <sup>-1</sup>	km s <sup>-1</sup>		km s <sup>-1</sup>
(1)	(2)	(3)	(4)	(5)	(6)
6538531393931377152	2460513.8887	-108.02 ± 0.92	-103.61 ± 7.37		4.41 ± 7.42
6538531393931377152	2460577.7344	-108.77 ± 0.33	-103.61 ± 7.37		5.16 ± 7.37
6538606396945476736	2460625.6136	-26.43 ± 0.30	-28.89 ± 3.38		2.46 ± 3.40
6565245300240135552	2460622.5947	-13.05 ± 0.36	-4.50 ± 4.19		8.55 ± 4.21
6574816067923362048	2460515.8217	28.68 ± 0.59	28.77 ± 3.55		0.09 ± 3.60
6597599529397812608	2460510.7758	-53.01 ± 0.12	-54.06 ± 2.19		1.05 ± 2.19
6597676048534977024	2460516.8058	92.48 ± 0.95	96.98 ± 8.86		4.50 ± 8.91
6597676048534977024	2460577.6767	88.07 ± 0.86	96.98 ± 8.86		8.91 ± 8.90
6597875094499505280	2460626.6193	-132.57 ± 0.33	-128.69 ± 5.22		3.88 ± 5.23
6598930556942930688	2460628.6493	-150.17 ± 0.35	-150.24 ± 12.97		0.07 ± 12.97
6605719555913798656	2460629.6017	72.45 ± 0.65	82.21 ± 4.66		9.76 ± 4.70
6623367718266041344	2460509.8637	-98.11 ± 0.44	-91.84 ± 6.43		6.27 ± 6.45
6626455181276398848	2460629.5844	71.45 ± 0.66	77.92 ± 4.81	SNR	6.47 ± 4.86
6635741587769528960	2460463.8002	24.58 ± 0.26	16.15 ± 4.11		8.43 ± 4.12
6636851819634037632	2460478.7667	218.38 ± 0.57	214.51 ± 7.08		3.87 ± 7.10
6639833007973763712	2460599.6325	-64.58 ± 0.24	-63.53 ± 2.22		1.05 ± 2.24
6640871668503771520	2460428.8454	-83.16 ± 0.18	-83.40 ± 2.12		0.24 ± 2.13
6645431961700136576	2460428.8285	-186.38 ± 0.66	-204.71 ± 7.70		18.33 ± 7.73
6645431961700136576	2460459.8064	-163.82 ± 0.77	-204.71 ± 7.70		40.89 ± 7.74
6645431961700136576	2460464.6628	-208.97 ± 0.60	-204.71 ± 7.70		4.26 ± 7.73
6645431961700136576	2460478.7980	-188.69 ± 0.80	-204.71 ± 7.70		16.02 ± 7.74
6645857438339795072	2460622.5528	155.87 ± 0.39	159.48 ± 4.54		3.61 ± 4.55
6646169837081308032	2460623.5227	313.32 ± 0.55	299.98 ± 7.59		13.34 ± 7.61
6647005122321157120	2460464.8188	77.87 ± 0.11	79.61 ± 3.06		1.74 ± 3.06
6647408196416540160	2460478.7302	59.44 ± 0.51	64.09 ± 9.66		4.65 ± 9.68
6657756868572776832	2460425.6664	150.28 ± 0.06	162.76 ± 3.37		12.48 ± 3.37
6657756868572776832	2460481.7712	154.72 ± 0.06	162.76 ± 3.37		8.04 ± 3.37
6661890173299322112	2460626.5243	-15.50 ± 0.16	-16.37 ± 7.51	SNR	0.87 ± 7.51
6675903066740376064	2460460.9081	-29.01 ± 0.11	-33.84 ± 1.83		4.83 ± 1.83
6685959341824044032	2460428.8625	-51.83 ± 0.32	-50.18 ± 2.92		1.65 ± 2.94
6688217566909990528	2460509.6584	33.09 ± 0.75	35.70 ± 8.20		2.61 ± 8.23
6689320926830067328	2460463.8430	10.56 ± 0.30	-2.82 ± 7.10		13.38 ± 7.11
6692958519311941760	2460462.8541	193.40 ± 0.20	192.80 ± 2.47		0.60 ± 2.48
6694977673633913728	2460460.8846	51.17 ± 0.12	55.07 ± 3.16		3.90 ± 3.16
6714154840051650560	2460627.5117	91.02 ± 0.41	64.23 ± 7.79		26.79 ± 7.80
6714154840051650560	2460633.5140	89.40 ± 1.05	64.23 ± 7.79	SNR	25.17 ± 7.86

**Table 3** *continued*

**Table 3** (*continued*)

<i>Gaia</i> DR3 ID	JD d	RV km s <sup>-1</sup>	<i>Gaia</i> DR3 Mean RV	Flags	RV Shift km s <sup>-1</sup>
			(4)		
(1)	(2)	(3)	(4)	(5)	(6)
6752999928728671104	2460509.7958	$38.72 \pm 0.35$	$45.11 \pm 5.52$		$6.39 \pm 5.53$
6753027107279926144	2460463.8675	$-39.69 \pm 0.30$	$-39.15 \pm 6.00$		$0.54 \pm 6.00$
6754940639769782400	2460464.8433	$-32.28 \pm 0.27$	$-35.55 \pm 5.55$		$3.27 \pm 5.55$
6769569470180424704	2460463.8181	$-21.54 \pm 0.47$	$64.26 \pm 10.26$		$85.80 \pm 10.27$
6769569470180424704	2460464.6870	$-23.40 \pm 0.42$	$64.26 \pm 10.26$		$87.66 \pm 10.27$
6769569470180424704	2460467.8426	$119.04 \pm 0.72$	$64.26 \pm 10.26$	SNR	$54.78 \pm 10.29$
6769569470180424704	2460478.8161	$-20.91 \pm 0.75$	$64.26 \pm 10.26$		$85.17 \pm 10.29$
6769569470180424704	2460479.7246	$-23.85 \pm 0.75$	$64.26 \pm 10.26$		$88.11 \pm 10.29$
6769569470180424704	2460480.6921	$-21.72 \pm 0.83$	$64.26 \pm 10.26$		$85.98 \pm 10.30$
6769569470180424704	2460515.7119	$-19.95 \pm 0.81$	$64.26 \pm 10.26$		$84.21 \pm 10.30$
6769569470180424704	2460517.7305	$-22.11 \pm 0.83$	$64.26 \pm 10.26$		$86.37 \pm 10.30$
6769569470180424704	2460518.7098	$-23.25 \pm 1.59$	$64.26 \pm 10.26$		$87.51 \pm 10.39$
6769569470180424704	2460519.6529	$-20.70 \pm 0.96$	$64.26 \pm 10.26$		$84.96 \pm 10.31$
6769569470180424704	2460532.7545	$-22.71 \pm 0.55$	$64.26 \pm 10.26$		$86.97 \pm 10.28$
6769569470180424704	2460555.7446	$-22.24 \pm 0.57$	$64.26 \pm 10.26$		$86.50 \pm 10.28$
6769569470180424704	2460559.7342	$-23.94 \pm 1.03$	$64.26 \pm 10.26$		$88.20 \pm 10.32$
6769569470180424704	2460559.7582	$-21.81 \pm 1.01$	$64.26 \pm 10.26$		$86.07 \pm 10.31$
6769569470180424704	2460570.5459	$-23.19 \pm 1.05$	$64.26 \pm 10.26$		$87.45 \pm 10.32$
6769569470180424704	2460580.6043	$86.46 \pm 1.40$	$64.26 \pm 10.26$	SNR	$22.20 \pm 10.36$
6769569470180424704	2460598.5582	$-22.29 \pm 1.76$	$64.26 \pm 10.26$		$86.55 \pm 10.41$
6769569470180424704	2460789.7973	$135.00 \pm 0.71$	$64.26 \pm 10.26$	SNR	$70.74 \pm 10.29$
6769569470180424704	2460790.8146	$-27.87 \pm 0.99$	$64.26 \pm 10.26$		$92.13 \pm 10.31$
6769569470180424704	2460815.8053	$-31.17 \pm 1.56$	$64.26 \pm 10.26$		$95.43 \pm 10.38$
6769569470180424704	2460843.6725	$-34.02 \pm 1.62$	$64.26 \pm 10.26$		$98.28 \pm 10.39$
6789503822144617216	2460480.8009	$-151.29 \pm 0.36$	$-149.52 \pm 6.11$		$1.77 \pm 6.12$
6790896731578064640	2460479.8226	$-207.41 \pm 0.41$	$-206.09 \pm 5.60$		$1.32 \pm 5.61$
6792552046335955456	2460624.5626	$-196.11 \pm 1.16$	$-170.97 \pm 4.63$	SNR	$25.14 \pm 4.78$
6797640173831774976	2460478.8590	$-33.17 \pm 0.41$	$-32.87 \pm 3.08$		$0.30 \pm 3.11$
6801546326327279104	2460479.8014	$-380.37 \pm 0.61$	$-380.52 \pm 7.91$		$0.15 \pm 7.94$
6803040081593000960	2460626.5702	$69.67 \pm 0.54$	$70.05 \pm 7.51$		$0.38 \pm 7.53$
6807367999878036736	2460627.5702	$-11.65 \pm 0.46$	$-13.35 \pm 4.51$		$1.70 \pm 4.53$
6812596551329038208	2460628.5256	$-5.99 \pm 0.40$	$-5.02 \pm 5.34$		$0.97 \pm 5.36$
6815475042707068672	2460625.5684	$-22.58 \pm 0.35$	$-25.68 \pm 3.88$		$3.10 \pm 3.89$
6820063064210514816	2460509.8212	$2.31 \pm 0.10$	$2.88 \pm 2.19$		$0.57 \pm 2.19$
6820303307501354496	2460628.6249	$-90.31 \pm 0.78$	$-106.92 \pm 7.46$		$16.61 \pm 7.50$
6822730754297502720	2460509.8396	$-17.67 \pm 0.27$	$-27.42 \pm 18.27$		$9.75 \pm 18.27$

**Table 3** *continued*

**Table 3** (*continued*)

<i>Gaia</i> DR3 ID	JD d	RV km s <sup>-1</sup>	<i>Gaia</i> DR3 Mean RV km s <sup>-1</sup>	Flags	RV Shift km s <sup>-1</sup>
(1)	(2)	(3)	(4)	(5)	(6)
6822730754297502720	2460628.6005	$-11.79 \pm 0.95$	$-27.42 \pm 18.27$		$15.63 \pm 18.30$
6823445986611497728	2460626.5949	$-4.92 \pm 0.25$	$-9.62 \pm 4.91$		$4.70 \pm 4.92$
6829836378256275072	2460478.9102	$11.75 \pm 0.08$	$11.87 \pm 1.23$		$0.12 \pm 1.23$
6834540436892911488	2460625.5513	$-77.89 \pm 0.20$	$-75.97 \pm 2.22$		$1.92 \pm 2.23$
6835881321387391872	2460480.7802	$13.16 \pm 0.16$	$15.17 \pm 2.03$		$2.01 \pm 2.04$
6843620100836059008	2460561.6018	$-263.48 \pm 0.03$	$-270.11 \pm 5.70$		$6.63 \pm 5.70$
6857258511787349632	2460478.8757	$-30.48 \pm 0.23$	$-24.93 \pm 2.67$		$5.55 \pm 2.68$
6864981928139773696	2460478.8409	$-47.57 \pm 0.47$	$-41.81 \pm 6.64$		$5.76 \pm 6.65$
6897453324003046784	2460479.8392	$15.27 \pm 0.10$	$16.26 \pm 4.78$		$0.99 \pm 4.79$
6903293654893289856	2460462.8852	$-262.57 \pm 0.07$	$-272.92 \pm 1.17$		$10.35 \pm 1.17$

## REFERENCES

- Abbott, B. P., Abbott, R., Abbott, T. D., et al. 2017, ApJL, 848, L12, doi: [10.3847/2041-8213/aa91c9](https://doi.org/10.3847/2041-8213/aa91c9)
- Abbott, R., Abbott, T. D., Acernese, F., et al. 2023, Physical Review X, 13, 041039, doi: [10.1103/PhysRevX.13.041039](https://doi.org/10.1103/PhysRevX.13.041039)
- Abdurro'uf, Accetta, K., Aerts, C., et al. 2022, ApJS, 259, 35, doi: [10.3847/1538-4365/ac4414](https://doi.org/10.3847/1538-4365/ac4414)
- Andrae, R., Rix, H.-W., & Chandra, V. 2023, The Astrophysical Journal Supplement Series, 267, 8, doi: [10.3847/1538-4365/acd53e](https://doi.org/10.3847/1538-4365/acd53e)
- Andrew, S., Penoyre, Z., Belokurov, V., Evans, N. W., & Oh, S. 2022, MNRAS, 516, 3661, doi: [10.1093/mnras/stac2532](https://doi.org/10.1093/mnras/stac2532)
- Andrews, J. J., Taggart, K., & Foley, R. 2022, doi: [10.48550/arXiv.2207.00680](https://doi.org/10.48550/arXiv.2207.00680)
- Astropy Collaboration, Robitaille, T. P., Tollerud, E. J., et al. 2013, Astronomy and Astrophysics, 558, A33, doi: [10.1051/0004-6361/201322068](https://doi.org/10.1051/0004-6361/201322068)
- Astropy Collaboration, Price-Whelan, A. M., Sipőcz, B. M., et al. 2018, The Astronomical Journal, 156, 123, doi: [10.3847/1538-3881/aabc4f](https://doi.org/10.3847/1538-3881/aabc4f)
- Astropy Collaboration, Price-Whelan, A. M., Lim, P. L., et al. 2022, ApJ, 935, 167, doi: [10.3847/1538-4357/ac7c74](https://doi.org/10.3847/1538-4357/ac7c74)
- Balbinot, E., Dodd, E., Matsuno, T., et al. 2024, Astronomy and Astrophysics, 687, L3, doi: [10.1051/0004-6361/202450425](https://doi.org/10.1051/0004-6361/202450425)
- Bashi, D., & Tokovinin, A. 2024, A&A, 692, A247, doi: [10.1051/0004-6361/202452637](https://doi.org/10.1051/0004-6361/202452637)
- Bennett, M., & Bovy, J. 2019, Modern Notices of the Royal Astronomical Society, 482, 1417, doi: [10.1093/mnras/sty2813](https://doi.org/10.1093/mnras/sty2813)
- Bernstein, R., Shectman, S. A., Gunnels, S. M., Mochnacki, S., & Athey, A. E. 2003, in Society of Photo-Optical Instrumentation Engineers (SPIE) Conference Series, Vol. 4841, Instrument Design and Performance for Optical/Infrared Ground-based Telescopes, ed. M. Iye & A. F. M. Moorwood, 1694–1704, doi: [10.1117/12.461502](https://doi.org/10.1117/12.461502)
- Brahm, R., Jordán, A., & Espinoza, N. 2017, Publications of the Astronomical Society of the Pacific, 129, 034002, doi: [10.1088/1538-3873/aa5455](https://doi.org/10.1088/1538-3873/aa5455)
- Buder, S., Sharma, S., Kos, J., et al. 2021, Modern Notices of the Royal Astronomical Society, 506, 150, doi: [10.1093/mnras/stab1242](https://doi.org/10.1093/mnras/stab1242)
- Chakrabarti, S., Simon, J. D., Craig, P. A., et al. 2023, The Astronomical Journal, 166, 6, doi: [10.3847/1538-3881/accf21](https://doi.org/10.3847/1538-3881/accf21)
- Chawla, C., Chatterjee, S., Breivik, K., et al. 2022, The Astrophysical Journal, 931, 107, doi: [10.3847/1538-4357/ac60a5](https://doi.org/10.3847/1538-4357/ac60a5)
- Chen, T., & Guestrin, C. 2016, in Proceedings of the 22nd ACM SIGKDD International Conference on Knowledge Discovery and Data Mining, 785–794
- Choi, J., Dotter, A., Conroy, C., et al. 2016, The Astrophysical Journal, 823, 102, doi: [10.3847/0004-637X/823/2/102](https://doi.org/10.3847/0004-637X/823/2/102)

- Corral-Santana, J. M., Casares, J., Muñoz-Darias, T., et al. 2016, *Astronomy and Astrophysics*, 587, A61, doi: [10.1051/0004-6361/201527130](https://doi.org/10.1051/0004-6361/201527130)
- Deason, A. J., Belokurov, V., Koposov, S. E., & Lancaster, L. 2018, *ApJL*, 862, L1, doi: [10.3847/2041-8213/aad0ee](https://doi.org/10.3847/2041-8213/aad0ee)
- El-Badry, K. 2024, *New Astronomy Reviews*, 98, 101694, doi: [10.1016/j.newar.2024.101694](https://doi.org/10.1016/j.newar.2024.101694)
- El-Badry, K. 2024, *The Open Journal of Astrophysics*, 7, 38, doi: [10.33232/001c.117652](https://doi.org/10.33232/001c.117652)
- El-Badry, K. 2025, *The Open Journal of Astrophysics*, 8, 62, doi: [10.33232/001c.138448](https://doi.org/10.33232/001c.138448)
- El-Badry, K., Lam, C., Holl, B., et al. 2024, *The Open Journal of Astrophysics*, 7, 100, doi: [10.33232/001c.125461](https://doi.org/10.33232/001c.125461)
- El-Badry, K., & Rix, H.-W. 2022, *Monthly Notices of the Royal Astronomical Society*, 515, 1266, doi: [10.1093/mnras/stac1797](https://doi.org/10.1093/mnras/stac1797)
- El-Badry, K., Bland-Hawthorn, J., Wetzel, A., et al. 2018, *MNRAS*, 480, 652, doi: [10.1093/mnras/sty1864](https://doi.org/10.1093/mnras/sty1864)
- El-Badry, K., Rix, H.-W., Quataert, E., et al. 2023a, *Monthly Notices of the Royal Astronomical Society*, 518, 1057, doi: [10.1093/mnras/stac3140](https://doi.org/10.1093/mnras/stac3140)
- El-Badry, K., Rix, H.-W., Cendes, Y., et al. 2023b, *Monthly Notices of the Royal Astronomical Society*, 521, 4323, doi: [10.1093/mnras/stad799](https://doi.org/10.1093/mnras/stad799)
- El-Badry, K., Simon, J. D., Reggiani, H., et al. 2024a, *The Open Journal of Astrophysics*, 7, 27, doi: [10.33232/001c.116675](https://doi.org/10.33232/001c.116675)
- El-Badry, K., Rix, H.-W., Latham, D. W., et al. 2024b, *The Open Journal of Astrophysics*, 7, 58, doi: [10.33232/001c.121261](https://doi.org/10.33232/001c.121261)
- Eyer, L., Audard, M., Holl, B., et al. 2023, *Astronomy and Astrophysics*, 674, A13, doi: [10.1051/0004-6361/202244242](https://doi.org/10.1051/0004-6361/202244242)
- Fulton, B. J., Weiss, L. M., Sinukoff, E., et al. 2015, *ApJ*, 805, 175, doi: [10.1088/0004-637X/805/2/175](https://doi.org/10.1088/0004-637X/805/2/175)
- Gaia Collaboration, Prusti, T., de Bruijne, J. H. J., et al. 2016, *Astronomy and Astrophysics*, 595, A1, doi: [10.1051/0004-6361/201629272](https://doi.org/10.1051/0004-6361/201629272)
- Gaia Collaboration, Brown, A. G. A., Vallenari, A., et al. 2018, *A&A*, 616, A1, doi: [10.1051/0004-6361/201833051](https://doi.org/10.1051/0004-6361/201833051)
- Gaia Collaboration, Vallenari, A., Brown, A. G. A., et al. 2023a, *Astronomy and Astrophysics*, 674, A1, doi: [10.1051/0004-6361/202243940](https://doi.org/10.1051/0004-6361/202243940)
- Gaia Collaboration, Arenou, F., Babusiaux, C., et al. 2023b, *Astronomy and Astrophysics*, 674, A34, doi: [10.1051/0004-6361/202243782](https://doi.org/10.1051/0004-6361/202243782)
- Gaia Collaboration, Panuzzo, P., Mazeh, T., et al. 2024, *Astronomy and Astrophysics*, 686, L2, doi: [10.1051/0004-6361/202449763](https://doi.org/10.1051/0004-6361/202449763)
- Gomel, R., Mazeh, T., Faigler, S., et al. 2023, *Astronomy and Astrophysics*, 674, A19, doi: [10.1051/0004-6361/202243626](https://doi.org/10.1051/0004-6361/202243626)
- GRAVITY Collaboration, Abuter, R., Amorim, A., et al. 2018, *Astronomy and Astrophysics*, 615, L15, doi: [10.1051/0004-6361/201833718](https://doi.org/10.1051/0004-6361/201833718)
- Green, G. M., Schlafly, E., Zucker, C., Speagle, J. S., & Finkbeiner, D. 2019, *The Astrophysical Journal*, 887, 93, doi: [10.3847/1538-4357/ab5362](https://doi.org/10.3847/1538-4357/ab5362)
- Halbwachs, J.-L., Pourbaix, D., Arenou, F., et al. 2023, *Astronomy and Astrophysics*, 674, A9, doi: [10.1051/0004-6361/202243969](https://doi.org/10.1051/0004-6361/202243969)
- Holl, B., Sozzetti, A., Sahlmann, J., et al. 2023, *A&A*, 674, A10, doi: [10.1051/0004-6361/202244161](https://doi.org/10.1051/0004-6361/202244161)
- Howard, A. W., Johnson, J. A., Marcy, G. W., et al. 2010, *ApJ*, 721, 1467, doi: [10.1088/0004-637X/721/2/1467](https://doi.org/10.1088/0004-637X/721/2/1467)
- Iorio, G., Torniamenti, S., Mapelli, M., et al. 2024, *A&A*, 690, A144, doi: [10.1051/0004-6361/202450531](https://doi.org/10.1051/0004-6361/202450531)
- Katz, D., Sartoretti, P., Guerrier, A., et al. 2023, *A&A*, 674, A5, doi: [10.1051/0004-6361/202244220](https://doi.org/10.1051/0004-6361/202244220)
- Kaufer, A., Stahl, O., Tubbesing, S., et al. 1999, *The Messenger*, 95, 8
- Kelson, D. D. 2003, *Publications of the Astronomical Society of the Pacific*, 115, 688, doi: [10.1086/375502](https://doi.org/10.1086/375502)
- Kelson, D. D., Illingworth, G. D., van Dokkum, P. G., & Franx, M. 2000, *The Astrophysical Journal*, 531, 159, doi: [10.1086/308445](https://doi.org/10.1086/308445)
- Klencki, J., Nelemans, G., Istrate, A. G., & Pols, O. 2020, *Astronomy and Astrophysics*, 638, A55, doi: [10.1051/0004-6361/202037694](https://doi.org/10.1051/0004-6361/202037694)
- Kroupa, P. 2001, *Modern Notices of the Royal Astronomical Society*, 322, 231, doi: [10.1046/j.1365-8711.2001.04022.x](https://doi.org/10.1046/j.1365-8711.2001.04022.x)
- Kurucz, R. L. 1979, *The Astrophysical Journal Supplement Series*, 40, 1, doi: [10.1086/190589](https://doi.org/10.1086/190589)
- Kurucz, R. L. 1993, *SYNTHE spectrum synthesis programs and line data*
- Lam, C. Y., El-Badry, K., & Simon, J. D. 2025, *ApJ*, 987, 215, doi: [10.3847/1538-4357/addac2](https://doi.org/10.3847/1538-4357/addac2)
- Lam, C. Y., Lu, J. R., Udalski, A., et al. 2022, *The Astrophysical Journal*, 933, L23, doi: [10.3847/2041-8213/ac7442](https://doi.org/10.3847/2041-8213/ac7442)
- Lindgren, L. 2018, [http://www.rssd.esa.int/doc\\_fetch.php?id=3757412](http://www.rssd.esa.int/doc_fetch.php?id=3757412)
- Lindgren, L. 2022, [https://dms.cosmos.esa.int/COSMOS/doc\\_fetch.php?id=1566327](https://dms.cosmos.esa.int/COSMOS/doc_fetch.php?id=1566327)
- Maeder, A. 1987, *Astronomy and Astrophysics*, 178, 159
- Marchant, P., Langer, N., Podsiadlowski, P., Tauris, T. M., & Moriya, T. J. 2016, *Astronomy and Astrophysics*, 588, A50, doi: [10.1051/0004-6361/201628133](https://doi.org/10.1051/0004-6361/201628133)

- Marín Pina, D., Rastello, S., Gieles, M., et al. 2024, A&A, 688, L2, doi: [10.1051/0004-6361/202450460](https://doi.org/10.1051/0004-6361/202450460)
- Mészáros, S., Bohlin, R., Allende Prieto, C., et al. 2024, A&A, 688, A197, doi: [10.1051/0004-6361/202449306](https://doi.org/10.1051/0004-6361/202449306)
- Mowlavi, N., Holl, B., Lecoeur-Taïbi, I., et al. 2023, Astronomy and Astrophysics, 674, A16, doi: [10.1051/0004-6361/202245330](https://doi.org/10.1051/0004-6361/202245330)
- Nagarajan, P., El-Badry, K., Lam, C., & Reggiani, H. 2024a, Publications of the Astronomical Society of the Pacific, 136, 074202, doi: [10.1088/1538-3873/ad5dfd](https://doi.org/10.1088/1538-3873/ad5dfd)
- Nagarajan, P., El-Badry, K., Rodriguez, A. C., van Roestel, J., & Roulston, B. 2023, Monthly Notices of the Royal Astronomical Society, 524, 4367, doi: [10.1093/mnras/stad2130](https://doi.org/10.1093/mnras/stad2130)
- Nagarajan, P., El-Badry, K., Triaud, A. H. M. J., et al. 2024b, Publications of the Astronomical Society of the Pacific, 136, 014202, doi: [10.1088/1538-3873/ad1ba7](https://doi.org/10.1088/1538-3873/ad1ba7)
- Nagarajan, P., El-Badry, K., Chawla, C., et al. 2025, PASP, 137, 044202, doi: [10.1088/1538-3873/adc839](https://doi.org/10.1088/1538-3873/adc839)
- Olejak, A., Belczynski, K., Bulik, T., & Sobolewska, M. 2020, Astronomy and Astrophysics, 638, A94, doi: [10.1051/0004-6361/201936557](https://doi.org/10.1051/0004-6361/201936557)
- Portegies Zwart, S. F., Verbunt, F., & Ergma, E. 1997, Astronomy and Astrophysics, 321, 207, doi: [10.48550/arXiv.astro-ph/9701037](https://doi.org/10.48550/arXiv.astro-ph/9701037)
- Radovan, M. V., Cabak, G. F., Laiterman, L. H., Lockwood, C. T., & Vogt, S. S. 2010, in Ground-based and Airborne Instrumentation for Astronomy III, ed. I. S. McLean, S. K. Ramsay, & H. Takami, Vol. 7735, International Society for Optics and Photonics (SPIE), 77354K, doi: [10.1117/12.857726](https://doi.org/10.1117/12.857726)
- Reggiani, H., Schlaufman, K. C., Healy, B. F., Lothringer, J. D., & Sing, D. K. 2022, The Astronomical Journal, 163, 159, doi: [10.3847/1538-3881/ac4d9f](https://doi.org/10.3847/1538-3881/ac4d9f)
- Sahu, K. C., Anderson, J., Casertano, S., et al. 2022, The Astrophysical Journal, 933, 83, doi: [10.3847/1538-4357/ac739e](https://doi.org/10.3847/1538-4357/ac739e)
- Schmidt, M. 1963, Nature, 197, 1040, doi: [10.1038/1971040a0](https://doi.org/10.1038/1971040a0)
- Sestito, F., Buck, T., Starkenburg, E., et al. 2021, MNRAS, 500, 3750, doi: [10.1093/mnras/staa3479](https://doi.org/10.1093/mnras/staa3479)
- Shahaf, S., Bashi, D., Mazeh, T., et al. 2023, Monthly Notices of the Royal Astronomical Society, 518, 2991, doi: [10.1093/mnras/stac3290](https://doi.org/10.1093/mnras/stac3290)
- Slater, C. T., Nidever, D. L., Munn, J. A., Bell, E. F., & Majewski, S. R. 2016, ApJ, 832, 206, doi: [10.3847/0004-637X/832/2/206](https://doi.org/10.3847/0004-637X/832/2/206)
- Tanikawa, A., Hattori, K., Kawanaka, N., et al. 2023, The Astrophysical Journal, 946, 79, doi: [10.3847/1538-4357/acbf36](https://doi.org/10.3847/1538-4357/acbf36)
- Vogt, S. S., Radovan, M., Kibrick, R., et al. 2014, Publications of the Astronomical Society of the Pacific, 126, 359, doi: [10.1086/676120](https://doi.org/10.1086/676120)
- Xue, X.-X., Rix, H.-W., Ma, Z., et al. 2015, ApJ, 809, 144, doi: [10.1088/0004-637X/809/2/144](https://doi.org/10.1088/0004-637X/809/2/144)